JGR Oceans

Correspondence to:

F. Nilsen,
frank.nilsen@unis.no

Wind-Driven Variability in the Spitsbergen Polar Current and the Svalbard Branch Across the Yermak Plateau

Frank Nilsen[1,2] , **Eli Anne Ersdal**[1] , and **Ragnheid Skogseth**[1]

[1]The University Centre in Svalbard, Longyearbyen, Norway, [2]University of Bergen, Geophysical Institute, Bergen, Norway

Abstract The Yermak Plateau (YP) acts as a guidance or barrier for the West Spitsbergen Current (WSC), which either crosses the plateau or flows around it to enter the Arctic Ocean. Closer to the West Spitsbergen coast, the Spitsbergen Polar Current (SPC) also flows over the YP in a narrow passage between the Svalbard Branch (SB) and the coast. A 2-year ocean observing program combined with altimetry and re-analysis wind data has given new knowledge on the variability and dynamics of the SPC and SB. The variability in the SPC and SB is controlled by the sea surface pressure gradient driven by the wind stress along the West Spitsbergen coast and locally on the YP. A peak-to-peak volume transport variability of 0.8 Sv and a positive heat transport anomaly of 3 TW were found in the SPC. The variability in the SB is mainly controlled by the upstream wind stress curl field along the West Spitsbergen Shelf where the negative wind stress curl field force the barotropic WSC branch directly into the SB. The peak-to-peak variability in the SB can exceed 4 Sv and in January 2016, an episodic heat flux was estimated to be 10 TW. Hence, an increasing number of winter cyclones affecting Svalbard will increase the volume transport variability and pulses of warm water to the shelf areas north of Svalbard.

Plain Language Summary This study shows how the variability in the wind pattern over the western and northwestern part of the Spitsbergen continental shelf controls the variability of the West Spitsbergen Current (WSC) branches flowing over the Yermak Plateau (YP). The WSC can bifurcate into the Svalbard Branch (SB) as a direct route across the YP or continue to flow along the YP, depending on the wind forcing in the area. The Spitsbergen Polar Current (SPC), bringing cold Arctic Water north of Svalbard, also flows over the YP, but closer to the Svalbard coast. The flow variability in both the SPC and the SB is controlled by the sea surface pressure gradient, and by measuring the pressure changes at the sea floor along the YP, the corresponding changes in the currents could be detected. Episodes of large heat flux toward the Arctic Ocean, capable of melting a 1-m sea ice thickness over a large area in only matter of days, were calculated in connection to a strong windstorm in January 2016. This demonstrates that the heat flux controlled by the volume transport variation can significantly amplify the warming trend during years with anomalous atmospheric circulation patterns showing more frequent cyclones influencing Svalbard during winter.

1. Introduction

During the past four decades, the Arctic has warmed approximately two times as rapidly as the entire Northern Hemisphere (Francis & Vavrus, 2012; Serreze & Barry, 2011; Stroeve et al., 2012). In Svalbard, the warming during winter has been particularly strong over recent decades with 5–6 C increase in winter temperatures (Hanssen-Bauer et al., 2019). Recent changes in large-scale atmospheric circulation patterns have brought warm Atlantic Water (AW) from the West Spitsbergen Current (WSC) onto the West Spitsbergen Shelf (WSS) and further into the fjords even during winter (Cottier et al., 2007; F. Nilsen et al., 2008, 2016; Pavlov et al., 2013; Skogseth et al., 2020; Tverberg et al., 2019). This has halted sea ice from forming (Muckenhuber et al., 2016) and opened up large areas of ice-free waters west and north of Svalbard (Cottier et al., 2007; Onarheim et al., 2014; Tverberg et al., 2014) with a potential impact on the Arctic ecosystem (Berge et al., 2005; Hegseth & Tverberg, 2013). Reduction and thinning of sea ice north and east of Svalbard in recent years are consistent with global warming and have likely led to more wind-generated upward mixing of warm and saline AW from about 200 m depth, preventing the formation of sea ice (Ivanov et al., 2016).
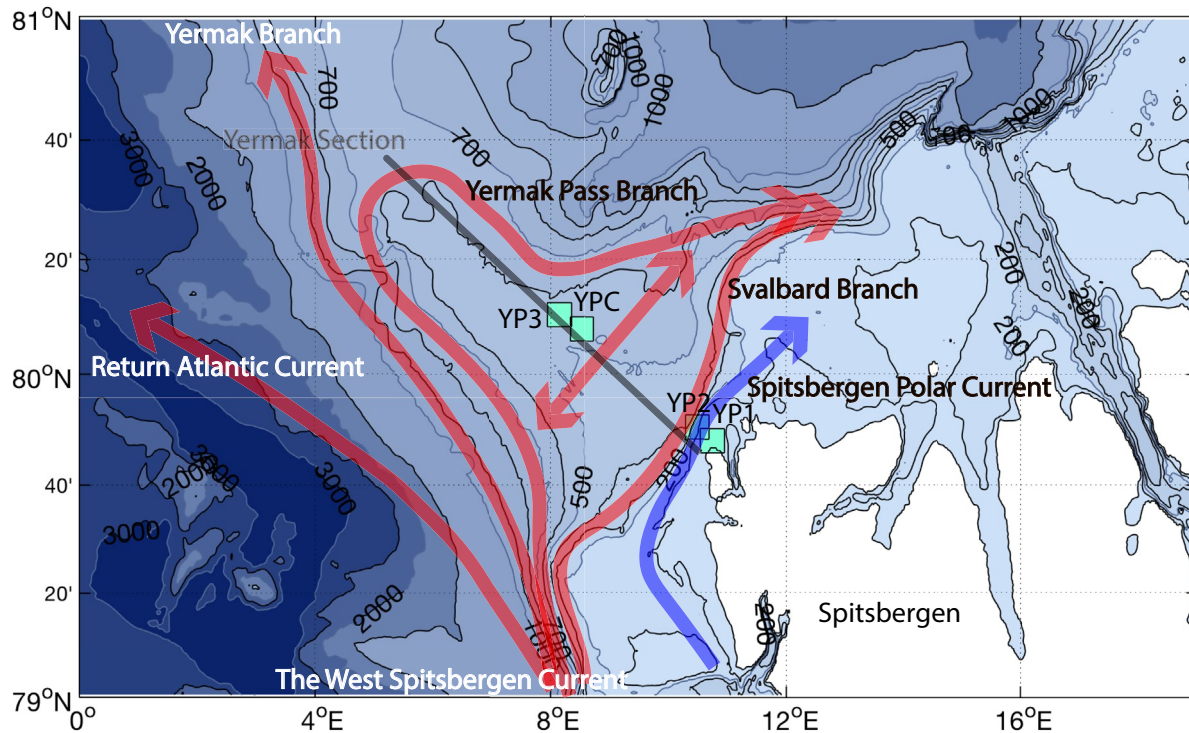
Figure 1. Topographic map over the southern Yermak Plateau (YP) at the northwestern corner of Spitsbergen with depth indication on the isobaths. The four REOCIRC moorings (YP1-3 and YPC) used in this study are marked with green boxes. This mooring section, and CTD profiles along this section, will be named the Yermak Section (dark gray line). The blue arrow indicates the fresh Spitsbergen Polar Current and the red arrows indicate the possible pathways of the AW around and across the YP described in the text.

Anomalies from the North Atlantic have been shown to propagate with the AW into the Nordic Seas, along the Norwegian coast into the Barents Sea through the Barents Sea Opening, and into the Arctic through the Fram Strait with the WSC (Årthun et al., 2017; Langehaug et al., 2018). The temperature and salinity of the inflowing waters to Fram Strait and to the Svalbard region have been particularly high after around 2,000 (González-Pola et al., 2018; Onarheim et al., 2014; Tverberg et al., 2019). Moreover, the core temperature of the AW entering the Arctic Ocean has increased in recent decades and Muilwijk et al. (2018) found that the variation in AW temperature dominates the heat transport in the WSC and the Fram Strait. North of 79°N, the WSC splits into four major branches (Figure 1: the Svalbard Branch [SB], the Yermak Pass Branch, the Yermak Branch, and the Return Atlantic Current [RAC]), but the roles of the different AW branches in the final heat transport into the Arctic Ocean are still not clear, especially on seasonal and annual time scales. The relative contribution from the different branches are important to know due to their different impact on the ocean climate, sea ice cover and surface air temperature, both regional and for the whole Arctic Ocean.

Although the Arctic Ocean is a deep ocean, the continental shelf area from the coastline out to the shelf break, make up as much as 52.9% of the total area in the Arctic Ocean (Jakobsson, 2002). The Fram Strait is seen as a deep open gate from the Nordic Seas into the Arctic Ocean, however, exchange is influenced by the shallow Yermak Plateau (YP) that is an extension of the Spitsbergen continental shelf toward Greenland, guiding different branches of warm AW. Hence, the YP exerts a dynamic control (topographic guiding) on the WSC branches, which must either cross the plateau or flow around it to enter the Arctic Ocean. Flow over or around the YP enhances the exchange with other water masses and the atmosphere, and heavily modifies the AW mass along these pathways. Recently, the branching and recirculation of the AW in the WSC have been studied in detail from model runs, both from an eddy-permitting model (Koenig et al., 2017) and an eddy-resolving model (Crews et al., 2019; Hattermann et al., 2016), where the model studies by Koenig et al. (2017) and Crews et al. (2019) suggested that the YPB is the main pathway by which AW in the WSC crosses the YP and enters the Arctic Ocean. Moreover, both model studies gave that the SB transport was less variable in time and lacked seasonality, with an average SB transport of 0.8 Sv for the eddy-resolving

model. On the contrary, in-situ measurements of the SB show that there is a large variability and seasonality in the SB (Morison, 1991) that will be further investigated here.

The density front between AW and Arctic Water (ArW) on the WSS and across the southeastern YP defines the West Spitsbergen Polar Front (WSPF). The Spitsbergen Polar Current (SPC), as first named by Helland-Hansen and Nansen (1909), is the coastal current associated with the WSPF along the west coast of Spitsbergen carrying ArW that originates from the Barents Sea and the Storfjorden area (Skogseth et al., 2020; Tverberg et al., 2019). As it flows northward, the SPC visits fjord mouths (F. Nilsen et al., 2008, 2016; Skogseth et al., 2020; Tverberg et al., 2019) and accumulate freshwater along the west coast of Spitsbergen, and finally, before it flows north of Svalbard, crosses the YP and the Yermak Section (Figure 1). Hence, the Yermak Section is the most suitable section for studying an integrated effect of freshwater discharged from land along the west coast and for seasonal variability in the SPC.

Here, the objective is to study the time variability and seasonality of the SPC and the SB on the YP, and the drivers of this variability. Emphasize is put on the wind forced volume transport variability of these currents, and connections are drawn toward the regional changing wind pattern and the increased number of winter cyclones influencing the Svalbard region on a larger scale. Moreover, no previous studies have described the dynamics and variability of the SPC in this area. This study is the first attempt in that respect by highlighting the important role the SPC has on modifying water masses and the sea ice cover north of Svalbard given the recent warming of the WSS (Cottier et al., 2007; F. Nilsen et al., 2008, 2016; Pavlov et al., 2013; Skogseth et al., 2020; Tverberg et al., 2019). The REOCIRC 2014–2016 measurement program on the YP was therefore designed to cover and monitor the flow variability of the SPC and the SB, and consisted of ocean bottom pressure (OBP) recorders, current meters, and temperature and salinity sensors. Here, we present results and theoretical considerations on the dynamics and active periods or strength of the SPC and the SB from 2 years of measurements with emphasis on wind-driven variability.

2. Measurements and Data

To reveal the flow dynamics across the YP and to gain a better understanding of the volume and heat flux variability across this Plateau, a set of in-situ ocean data and ocean climatology (UNIS HD; Skogseth et al. (2019)), together with reanalyzed atmospheric data (NORA10; Reistad et al., 2011) over a larger area, and altimetry data products (Ssalto/Duacs, CMEMS) over a larger time span, were synchronized in time and constitute a synopsis of different products presented for a common time period to study the seasonal and annual variability in ocean currents across the YP. Here, we list the different data sets used in the study, their accuracy, and the necessary adjustments and filtering needed to combine them.

2.1. Study Area

The YP is a relatively shallow submarine peninsula (600 m on average) starting from the northwestern corner of Spitsbergen as a north-northwestward extension of the Spitsbergen continental shelf (Figure 1), influencing the SPC and the different branches of the WSC before they enter the Arctic Ocean. Despite its northerly latitude from 79.5°N to 83°N, the water above the YP is periodically ice-free due to the combined effects of strong tidal currents (Hunkins, 1986; Padman et al., 1992) over the shallow bathymetry and the presence of warm AW, which induce mixing and heat release to the atmosphere (Fer et al., 2010, 2015). As a result, the open water at the southern part of the YP and north of Svalbard has been referred to as the Whaler's Bay (Onarheim et al., 2014).

The complicated topography of the Fram Strait causes the WSC to split (Figure 1) into three main branches around 79°N (Quadfasel et al., 1987). One branch recirculates westward (RAC) between 78°N and 81°N following the topographic fracture zones across the Fram Strait (Bourke et al., 1988; Teigen et al., 2011) and are largely driven by eddy relief from the slope region (Gascard et al., 1995; von Appen et al., 2016; Hattermann et al., 2016). As a continuation of the eastern baroclinic WSC branch, the Yermak Branch flows along the western slope of YP (Manley et al., 1992). The barotropic WSC branch continues as the SB (Aagaard et al., 1987; Manley et al., 1992), crosses the YP and reaches the Arctic Ocean. More precisely, the SB follows the 200–450 m isobaths of the WSS slope on the YP. Another more variable branch leading AW across the YP has been described by Gascard et al. (1995); the topographically guided Yermak Pass Branch was discovered

Table 1
The Details of Locations, Water Depths, and Instrument Distributed on Four REOCIRC Moorings on the Yermak Plateau Between 2014 and 2016

Mooring	Latitude	Longitude	Deployment depth [m]	Parameter
YP1	79° 47.958′	010° 44.75′	27/29	OBP, CTD
YP2	79° 50.442′	010° 29.60′	110/110	OBP, CTD
YP3	80° 10.467′	008° 08.71′	550/550	OBP, CTD
YPC	80° 07.100′	008° 32.04′	512/515	VT × 3, CTD × 3, T × 16

Measuring periods:

YP1–3, YPC: 28.08.2014–27.08.2015 and 28.08.2015–13.08.2016 (2 years).

OBP – Ocean bottom pressure measured with SBE 26plus 1 m above bottom.

VT – Velocity and Temperature by Aandreaa Seaguard (60 m) and RCM9 (200 and 500 m).

CTD – SBE 37 Microcat at YPC (80, 200, and 300 m) and 2 m above OBP.

T – Temperature by Vemco minilog II evenly distributed vertically (Figure 9).

Note. Figure 1 shows the positions of the four moorings.

during the ARCTEMIZ88 experiments. In our study, the focus is on the dynamics and variability of the SPC and the SB, and a monitoring program has been designed to capture the flow variability in response to external forcing and perturbation.

2.2. Mooring Time Series on the Yermak Plateau

From August 28, 2014 to August 13, 2016, OBP recorders (SBE 26plus) were measuring the weight of the water column above the ocean sea floor (Figure 1) at 29 m depth (YP1), 110 m depth (YP2), and 550 m depth (YP3). In addition, a current meter mooring (YPC) was deployed 8.8 km southeast of YP3 at 515 m depth. The YPC mooring was equipped with three current meters, one Aandreaa Seaguard (SG) at 60 m depth and two Aanderaa RCM9 positioned at 200 and 500 m depth. Three SBE 37 Microcat CTDs measured conductivity and temperature (80, 200, and 300 m depth) and 16 Vemco minilog II temperature loggers were distributed vertically along the mooring line. More details on the four moorings can be found in Table 1. YP1–3 were specially designed for OBP observations with a socket for the SBE 26plus rigidly attached to the anchor weight, in addition to a Microcat (SBE 37) CTD 3 m above the sea floor.

As shown in Figure 1, YP1 was about 2 km off the northwest corner of Spitsbergen (Amsterdamøya) in shallow water to capture the SPC (F. Nilsen et al., 2016; Skogseth et al., 2020; Tverberg et al., 2019), and separated from YP2 by about 6.7 km. The outer site (YP3) was about 66 km northwest of the coast. The YP2 and YP3 sites were established to compare the OBP time series with data from a similar measurement program from the early 80s (Morison, 1991). The two outer sites are separated by about 58 km and span a portion of the WSC that flows across the YP and into the Arctic Basin, that is, the SB (Aagaard et al., 1987; Manley et al., 1992).

In a local inverse barometer model, a rise(fall) of 1 mbar in air pressure results in a fall(rise) of 1 cm in sea level to within approximately half a percent (Wunsch & Stammer, 1997). However, in an ideal local inverse barometer situation, the sea level and air pressure contribution to ocean bottom pressure will cancel out. This gives less noise and residual variance compared to tide gauge records (measuring the surface water level), and OBP recorders are preferable to that of sea level for the determination of tidal parameters and for the detection of signals such as those due to small tsunamis (Pugh & Woodworth, 2014). For the study of wind-driven variability of the water column height, the measured OBP can be converted to water column thickness by dividing the OBP data with the specific weight ρg, where g is the gravity acceleration and ρ is an average water column density. Hence, we assume that the OBP variability due to wind-driven water column thickness variation occurs over a much shorter time scale than the variability of the OBP due to density variations. The latter is assumed to take place over a seasonal time scale while the wind-driven variability can occur on the order of hours. After the pressure-to-water-column-thickness conversion is performed, the time-mean water column thickness is subtracted from the whole time series, which gives us the
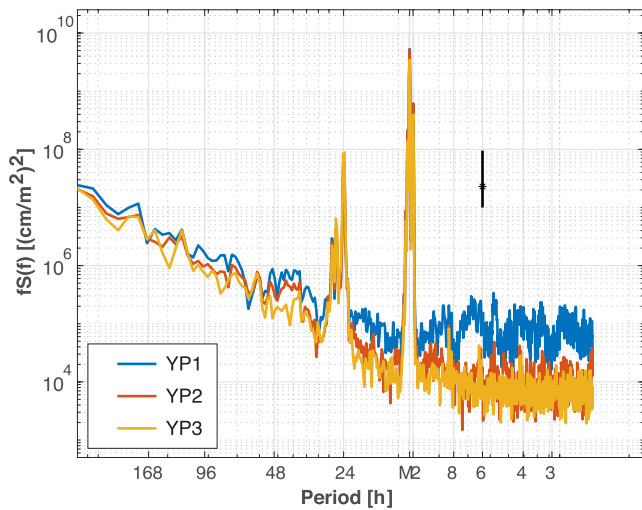
Figure 2. Power Spectra from the ocean bottom pressure (OBP) time series at the YP1, YP2, and YP3 (Figure 1). The 95% confidence interval is given by the vertical bar.

water column thickness anomaly that we use for calculations. Note that both water column thickness anomaly and OBP data/anomaly will be used when presenting the in situ measurements from the OBP recorders. The accuracy of the SBE 26plus quarts pressure sensor for a single measurement is ± 0.01% of the full sensor depth range. For the outer sensor at 550 m depth, the accuracy then becomes ± 0.055 m, while the inner mooring at 30 m depth has an accuracy of ± 0.003 m. Both 1 and 15 min sampling intervals were used during the measuring campaign, increasing the accuracy to be better than a millimeter. Moreover, the OBP data have been averaged into 1-h time intervals.

The tidal signal in the OBP data is significant (Figure 2), and the semidiurnal tidal energy is one order of magnitude larger than the diurnal tidal energy. These high-frequency tides (diurnal and semidiurnal) were subtracted from the OBP anomaly time series using a tidal time series based on harmonic analysis, and de-tided time series for each location can be seen in Figure 3. Differences in water thickness anomaly between the OBP recorders represent the variability in the geostrophic current across the Yermak Section, that is, the section along the YP1-3 and the YPC moorings. However, a correction due to the sloping sea floor is needed before bottom currents and geostrophic velocities can be calculated (Section 3.2).

In situ ocean currents and hydrography have been measured on the YPC mooring, 8.8 km southeast of YP3 (Table 1). Spikes in the temperature and salinity data have been identified and replaced by linearly interpolated values using a window size of 3.5 days and a threshold value of three standard deviations from the detrended mean. Temperature and salinity time series from moored instruments are calibrated from conductivity, temperature, and depth (CTD) profiles obtained at the start and end of the yearlong time series.
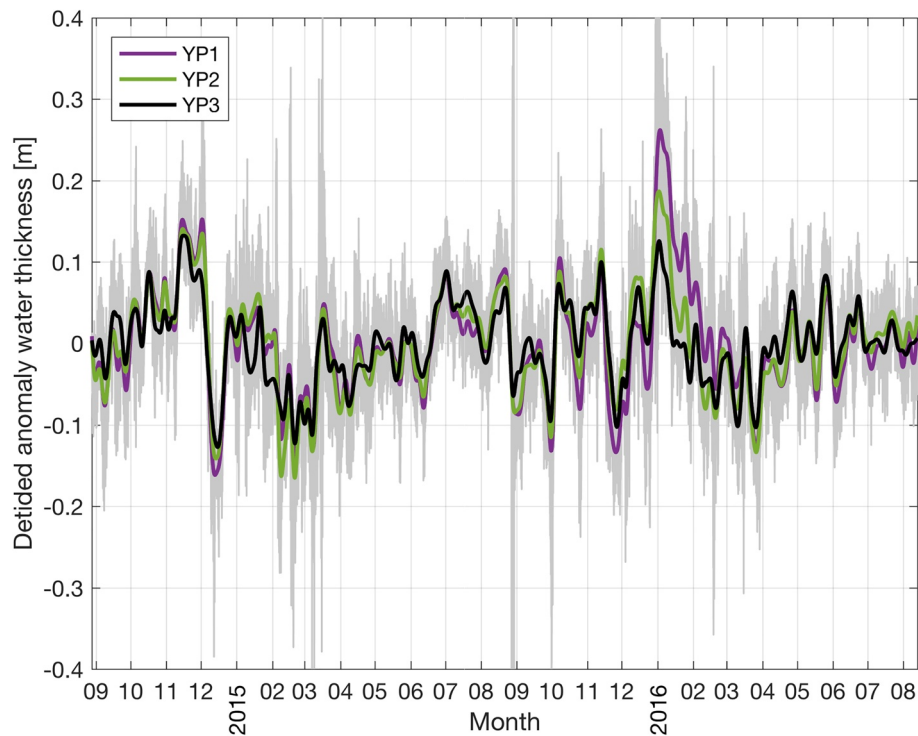

Figure 3. The water column thickness anomaly from the three ocean bottom pressure (OBP) recorders (YP1-3) along the Yermak Section after all the significant semidiurnal and diurnal tidal components have been subtracted. The bold curves represent 7 days running mean while the gray shading represents the raw data and variability.

Table 2
Water Masses and Their Temperature (T) and Salinity (S) Characteristics for the West Spitsbergen Shelf Adapted From Swift and Aagaard (1981), Loeng (1991), Svendsen et al. (2002), and Langehaug and Falck (2012)

Water Mass	T (°C)	S (psu)	S (gkg^{-1})
Atlantic Water (AW)	≥3	≥34.9	≥35.07
Transformed Atlantic Water (TAW)	1–3	34.7–34.9	34.87–35.07
Arctic Intermediate Water (AIW)	−1.1 to 0	34.7–34.92	
Arctic Water (ArW)[a]	≤0	34.4–34.8	34.46–34.97

Note. Salinity characteristics are given in both practical salinity unit (psu) and in absolute salinity (g/kg).
[a]ArW as defined for the Barents Sea.

Temperature time series from the Vemco loggers and Aanderaa current meters were adjusted from comparison with the temperature and salinity time series from the SeaBird SBE 37s that were mounted above and below the respective instruments during time periods with homogeneous water columns (wintertime). Water mass definitions used in the following and their temperature (*T*) and salinity (*S*) characteristics valid for the YP can be found in Table 2.

2.3. Historic Temperature and Salinity Data

We use the UNIS hydrographic database (UNIS HD; Skogseth et al., 2019) which is a collection of temperature and salinity profiles from UNIS student and research cruises around Svalbard (since 1994) compiled with hydrographic data from the same area (1–30°E and 75–81.5°N) in the Norwegian Marine Data Centre (NMDC, https://www.nmdc.no/), the International Council for the Exploration of the Sea (ICES) data set on ocean hydrography (https://ocean.ices.dk/HydChem/), the PANGAEA data publisher (https://www.pangaea.de/), and the database from the project Norwegian Iceland Seas Experiment (NISE; J. E. Nilsen et al., 2008). The UNIS HD data have been used to construct a mean summer hydrographic section for the YP and a downstream temperature gradient for the heat flux calculation.

2.4. NORA10 Reanalysis and Wind Stress Fields

Wind speed and direction (10 m above sea level) for every hour over the area around Svalbard (10°W–40°E, 76°N–83°N) were obtained from the Norwegian Reanalysis Archive (NORA10; Reistad et al., 2011) to calculate the wind stress components using Large and Pond (1981) parameterization, and to calculate the wind stress curl time series over and around the YP. NORA10 is a regional high-resolution (10–11 km) atmospheric downscaling of ERA-40 (Uppala et al., 2005) and ECMWF IFS (European Center for Medium-Range Weather Forecasts Integrated Forecasting System) operational analyses (after 2002), covering the northern North Atlantic, the Nordic Seas, and the Barents Sea. The dynamic atmospheric downscaling is performed as a series of short prognostic runs (using HIRLAM) initialized from a blend of ERA-40 and the previous prognostic run to preserve the fine-scale surface features from the high-resolution model while maintaining the large-scale synoptic field from ERA-40. Spatially averaged wind stress component time series (Figure 4a over the black box in Figure 4c) and a grid point wind stress curl time series (Figure 4b at the green triangle in Figure 4c), both representing the REOCIRC study area, are shown together with a map of the yearly averaged (2015) wind stress vectors and the wind stress curl field (Figure 4c).

2.5. Satellite Observations

Satellite data have been downloaded from the Copernicus Marine and Environment Monitoring Service (CMEMS; http://www.marine.copernicus.eu), more specifically, the altimetry products from Ssalto/Duacs (earlier AVISO) dating back to 1994. The downloaded product from CMEMS includes the CNES-CLS18 (1/8°) Mean Dynamic Topography (MDT). The MDT is the difference between the mean sea surface height (MSS) and the geopotential reference surface called the geoid (G), thus MDT = MSS-G. The geoid can be considered as the shape of an imaginary global ocean at rest, dictated by gravity in the absence of tides
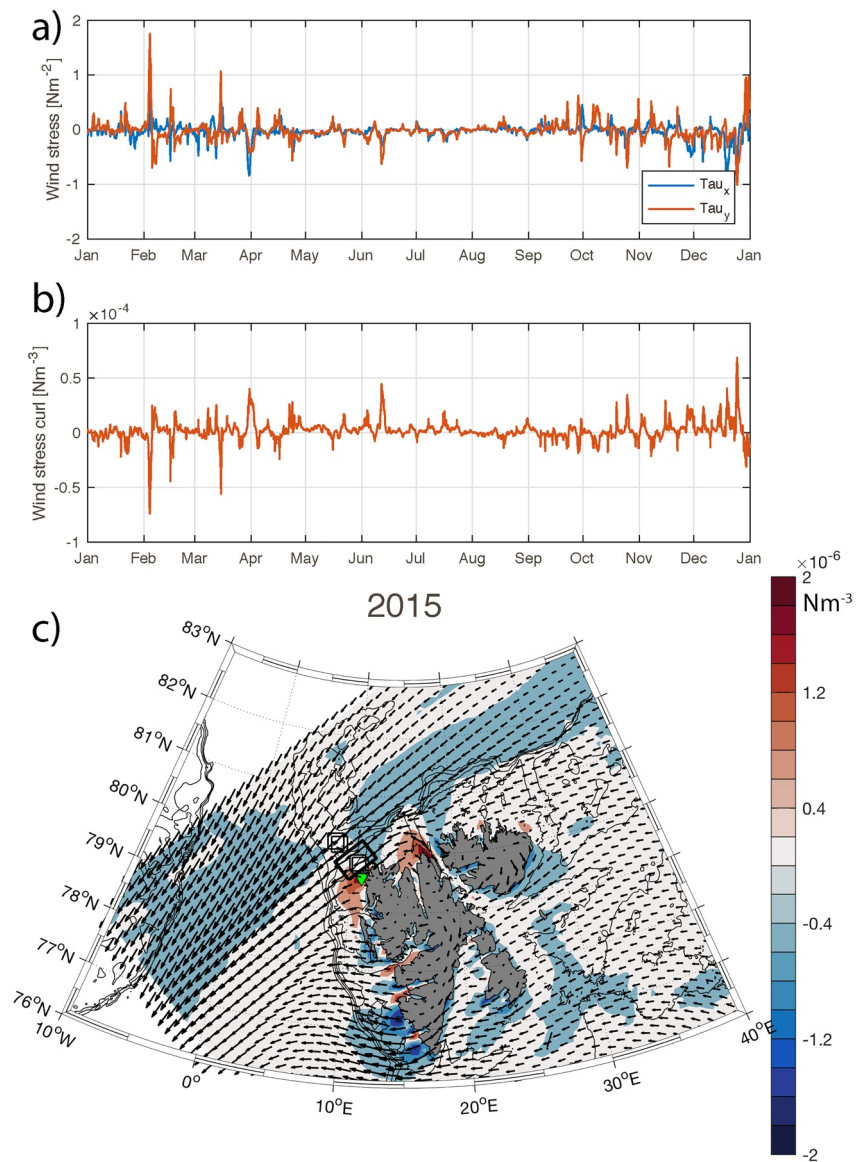
Figure 4. (a) The wind stress times series (2015) spatially averaged over the black box (in panel c), (b) The calculated wind tress curl time series from a single point (green triangle in c) close to the coast, and (c) The 2015 annual averaged wind stress vector and the contoured wind stress curl. The white squares in panel (c) are the ocean bottom pressure (OBP) moorings YP1-3 and the current meter mooring YPC.

and currents. It is a crucial reference for accurately measuring ocean circulation, sea-level change, and ice dynamics. Here, we use the MDT gridded product to calculate the surface current v_s (Figure 5) from the horizontal gradient of the sea surface elevation. Moreover, in order to use the absolute bottom velocity from the OBP data on the YP, the time-mean surface current between YP3 and YP2 has been estimated from the MDT data, $v_0 = 4.3 \, \text{cm s}^{-1}$.

3. Methods

3.1. Climatology From Historical Hydrographic Data

All available hydrographical profiles in summer (July–early October) within a distance of $\pm$ 0.2° latitude ($\pm$ 0.35° latitude west of 6.5°E) from the Yermak Section (Figure 1) were extracted from the UNIS HD (Skog-seth et al., 2019) to obtain mean summer hydrographic sections. In total, 305 hydrographic profiles were
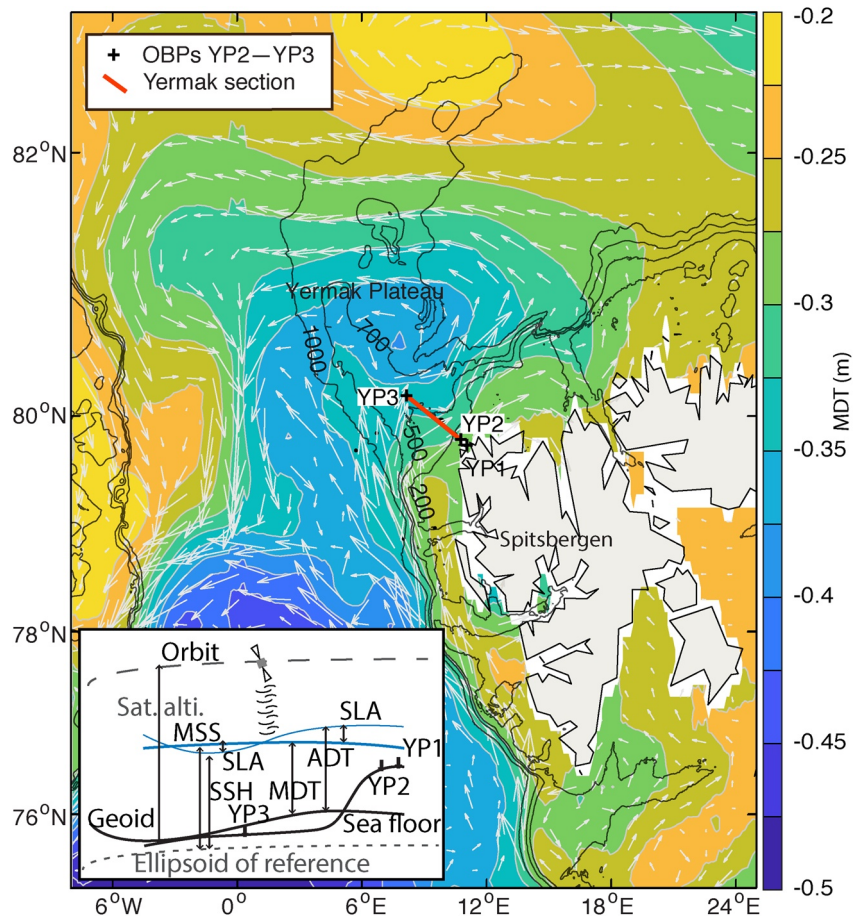
Figure 5. The bathymetry (black contour) in the Fram Strait together with the overlying MDT (CNES-CLS18 1/8°, filled colored contours). The geostrophic surface velocity vectors (v_s) calculated from the MDT gradient are also plotted (white arrows). The SB part of the Yermak Section is drawn with a red line between the ocean bottom pressure moorings YP2 and YP3 (+). The illustration in the lower left corner has been redrawn from the homepage: https://duacs.cls.fr/. The Mean Sea Surface (MSS) and the Sea Surface Height (SSH) relate to the ellipsoid of reference, while the Mean Dynamic Topography (MDT) and the Absolute Dynamic Topography (ADT) relate to the geoid. The Sea Level Anomaly (SLA) is the deviation from the mean.

used for the 2006– 2018 climatological summer sections. The profiles were first bin-averaged with the bin centers at the positions of the Yermak Section (repeated hydrographic stations indicated in Figures 1 and 6), and the bin size in the longitudinal direction was the half distance between two neighboring bin centers. Hence, the bins are tight in longitudinal direction with no gaps or overlaps. At the end points of the Yermak Section, profiles within 0.3° west (east) of the western (eastern) bin center were included in the bin average. Each profile was weighted with its distance to the bin center to produce weighted bin-averaged sections of temperature, salinity, and potential density anomaly with 1 m vertical resolution. The weighted bin-averaged sections were then interpolated onto a 500 m horizontal times 1 m vertical grid resolution using the kriging interpolation method from Golden Software Surfer 12 through the Matlab function surfergriddata.m, using Matlab version R2018b. Only bins with more than 2 years represented (to avoid any biases and assure good data coverage) were used in the kriging interpolation. Finally, in Figure 6, the interpolated sections were smoothed vertically with a low-pass filter to reduce any remaining noise.

3.2. Obtaining Bottom Geostrophic Current From OBP Measurements

There are a number of ways of relating water pressure difference to geostrophic current. The simplest expression is that for an interior steady state flow field
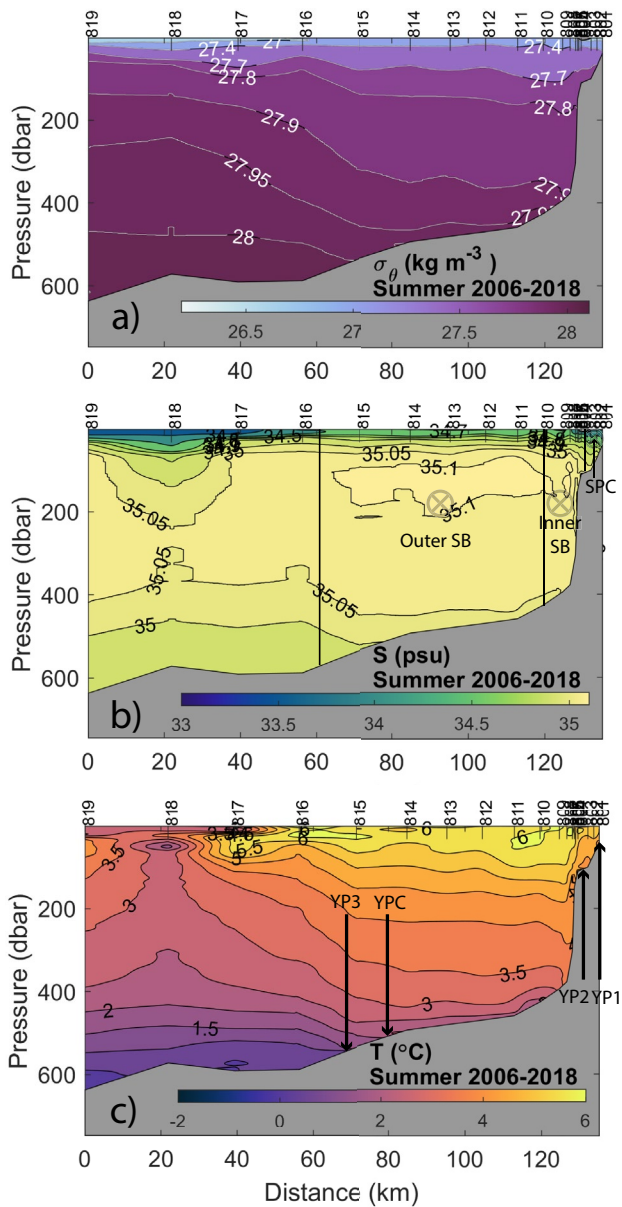
Figure 6. Summer hydrographic climatology for the Yermak Section in the 2006–2018 period; (a) Calculated potential density (σ_θ) with the sea surface as the reference level, (b) Bin-averaged and interpolated (kriging) salinity with the illustration of the governing current structure in the Yermak Section, and (c) Bin-averaged and interpolated (kriging) temperature where the position of the REOCIRC moorings are indicated. Hydrographic station numbers in the Yermak Section (Figure 1) are shown in the top of each figure.

$$v_g = \frac{1}{\rho_0 f} \frac{\partial p}{\partial x}, \tag{1}$$

where x, y, and z comprises a right-handed coordinate system with z positive up, v is the velocity in the y direction across the Yermak Section (Figure 1), p is the pressure, ρ_0 is the reference density, and f is the Coriolis parameter. The measurements discussed here were made on a sloping bottom in a non-homogeneous fluid, so these complications must be evaluated. A hydrostatic balance is assumed in the vertical and an expression for the pressure can be found by integrating the hydrostatic balance upward from the bottom ($z = -H(x,y)$) to some depth z

$$p = -g \int_{-H}^{z} \rho \, dz + p_b, \tag{2}$$

where g is the gravity acceleration, ρ is the density, and $p_b = p(t,x,y,-H)$ is the bottom pressure. Inserting this expression for p into the geostrophic balance (Equation 1), and by making use of Leibnitz's rule for differentiation of integral (e.g., Aaboe & Nøst, 2008), the geostrophic velocity, v_g, can be given in the following form

$$v_g(z) = -\frac{g}{\rho_0 f} \int_{-H}^{z} \frac{\partial \rho}{\partial x} dz - \frac{g}{\rho_0 f} \rho_b \frac{\partial H}{\partial x} + \frac{1}{\rho_0 f} \frac{\partial p_b}{\partial x} = v_t + v_b, \tag{3}$$

where $\rho_b = \rho(t,x,y,-H)$ is the bottom density. The first term on the right hand side of Equation 3 is the depth integrated thermal wind y-component, v_t, with zero velocity at the bottom and the two last terms constitute the geostrophic bottom velocity v_b.

3.2.1. The Geostrophic Bottom Velocity

The sum of the last two terms in Equation 3 makes up the geostrophic bottom velocity

$$v_b = -\frac{g}{\rho_0 f} \rho_b \frac{\partial H}{\partial x} + \frac{1}{\rho_0 f} \frac{\partial p_b}{\partial x}. \tag{4}$$

This equation for the bottom current is close to the geostrophic balance in form, except for the bottom density term, $\frac{g}{\rho_0 f} \rho_b \frac{\partial H}{\partial x}$, which is a weight and pressure correction since the measurements were done on a sloping bottom in a non-homogeneous fluid. The significance of this term is best illustrated by integrating v_b in the horizontal distance L along the section where we find an expression for the horizontal averaged bottom current over L. Before integration, it is useful to first split up the bottom density in a density anomaly part, ρ_b', and a constant reference density for each isobath, $\rho_r = \rho_r(H)$, that is, $\rho_b = \rho_b' + \rho_r(H)$. This is convenient since the OBP recorders measure the fluctuation around a mean, and a velocity estimate will be made by calculating the difference between the shallow ($-H_1$ at x_1) and deep ($-H_2$ at x_2) pressure anomalies measured at the bottom. As will become clear, the first term on the right side in Equation 4 compensate for the difference in the weight of the water column at x_1 and x_2, and the fluctuation of this weight in time. Since we subtract the mean pressure from each measured time series, the reference density part ρ_r of ρ_b in Equation 4 can be disregarded and we are left with a steric pressure term including ρ_b'. The horizontal averaged bottom current anomaly, $\overline{v_b'}$, averaged over a distance L between x_1 and x_2, can now be expressed as

$$\rho_0 f \overline{v_b'} = \frac{1}{L} \left(\int_{x_2}^{x_1} (-g\rho_b') \frac{\partial H}{\partial x} dx + \int_{x_2}^{x_1} \frac{\partial p_b}{\partial x} dx \right) = \frac{1}{L} \left(p_b^1 - p_b^2 \right) - \frac{1}{L} \int_{x_2}^{x_1} g\rho_b' \frac{\partial H}{\partial x} dx. \tag{5}$$
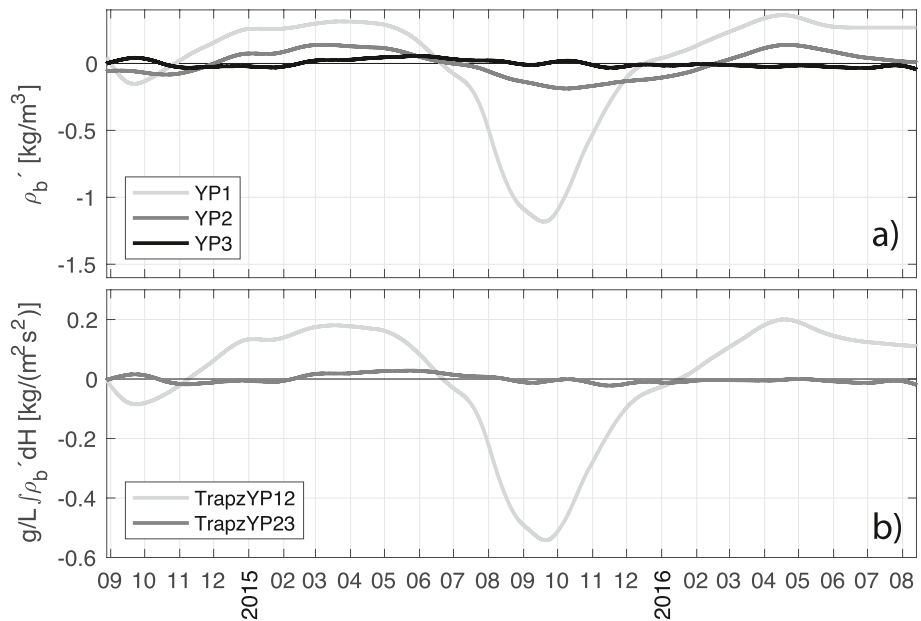
Figure 7. (a) The density anomaly time series at YP1–YP3, that is, the deviation from the constant reference density for each isobath, $\rho_r(H)$, calculated from the density time series recorded 3 m above the sea floor at the YP moorings. (b) The approximated integration (second term in Equation 7) is calculated based on observations from YP3 and YP2 (dark gray) to YP2 and YP1 (light gray).

Making the substitution $dH = \frac{\partial H}{\partial x}dx$, that is, from distance along the x-axis to water column thickness, converts the last term in Equation 5 into a steric pressure form

$$\rho_0 f\overline{v_b'} = \frac{\Delta p_b}{L} + \frac{1}{L}\int_{H_1}^{H_2}g\rho_b'dH, \tag{6}$$

where $\rho_b' = \rho_b - \rho_r(H)$ is calculated from the bottom density measurements. Since we only have observations from H_1 at x_1 and H_2 at x_2, the definite integral will be approximated by using the trapezoidal approximation technique,

$$\rho_0 f\overline{v_b'} = \frac{\Delta p_b}{L} + \frac{g}{L}\frac{\rho_{b1}' + \rho_{b2}'}{2}\left(H_2 - H_1\right) = \rho_0 f\left(\overline{v_{dP}} + \overline{v_{b\rho}}\right). \tag{7}$$

Adding the weight correction along the sea floor, $\overline{v_{b\rho}}$, between the shallow and deep OBP recorders (second term), to the in situ OBP difference in the first term, $\overline{v_{dP}}$, it is now possible to estimate the variability of the bottom velocity (Equation 7) between the three OBP time series. Moreover, the barotropic transport variability across the Yermak Section can then be estimated from the section averaged bottom velocity variability (Equation 7) multiplied by the section area. If the flow is barotropic, that is, $\frac{\partial \rho}{\partial x}$ is zero, the anomalous bottom velocity becomes the anomalous geostrophic current and accounts for all the flow variability. Finally, if the bottom is flat, the bottom density term ($\overline{v_{b\rho}}$) is zero. Hence, the bottom density term serves as a correction to the bottom pressure difference term.

The bottom density term in Equation 7, $\overline{v_{b\rho}}$, corrects for the deviation in the density of water between the two depths where the pressure measurements are made. The density anomaly in Figure 7a is the deviation from the constant reference density for each isobath, $\rho_r(H)$, calculated by taking the mean of the density time series recorded at the sea floor. A positive value indicates a denser water mass than the reference density, typically during winter, and a negative value means a less dens water mass at the location. Using the time series in Figure 7a, an integration along the sea floor in Equation 7 can be done as an approximation through some assumptions knowing the climatological and seasonal hydrographic spatial pattern on the YP; from CTD sections (Figure 6), it is clear that the YP2 bottom density time series can only represent a small part of the section between YP2 and YP3, that is, from YP2 (109 m depth) down to approximately 200 m depth (Figure 6a). Moreover, the YP3 time series might represent the bottom density variation from

200 m depth down to YP3 (549 m depth), where the bottom density at YP3 can have an offset of around 0.1 kgm^{-3} (compared to 250 m depth) in summer, and none in winter (not shown). Hence, the integration of the bottom density from YP2 to YP3 (Figure 7b) was done from YP2 toward 200 m depth using the YP2 and YP3 data, and from 200 m depth to YP3 using YP3 data only. The different integrals were weighted with their depth level difference, respectively. The integral from YP1 to YP2 was done without dividing the integral into several sections. Results from the integration between the OBP recorders are seen in Figure 7b, and relative to the geostrophic bottom velocity between YP2 and YP3, the dark gray line in Figure 7b represents the underestimation or overestimation of the pressure difference between those two positions (in situ pressure) due to the variation in the weight of the water mass below YP2 and between YP2 and YP3. A positive bottom density anomaly between YP2 and YP3 in spring 2015 (Figure 7), imply that the observed anomalous ocean bottom pressure difference estimated from time series recorded at two different bottom depths ($\overline{v_{dP}}$ in Equation 7) has to be increased ($\overline{v_{b\rho}}$) due to the increased water column weight below the YP2 depth level. Hence, the weight anomaly compensation ensures that the pressure gradient ($\Delta P/\Delta x$) represents a constant depth level for the bottom geostrophic velocity anomaly $\overline{v_b'}$ between YP2 and YP3, although the pressure time series are recorded in different depth levels on a sloping seafloor.

3.2.2. Thermal Wind and Geostrophic Velocity

To compare the thermal wind velocity v_t in Equation 3 with the bottom geostrophic velocity anomaly variability in Equation 7, we need to perform the same horizontal integration or averaging,

$$\overline{v_t(z)} = -\frac{g}{\rho_0 fL}\int_{x_2}^{x_1}\int_{-H}^{z}\frac{\partial\rho}{\partial x}\,dzdx. \tag{8}$$

Splitting up the vertical integration from the YP3 bottom depth (H_2) to the YP2 bottom depth (H_1) and the remaining water column up to the depth level z result in

$$\overline{v_t(z)} = -\frac{g}{\rho_0 fL}\int_{x_2}^{x_1}\left[\int_{-H_2}^{-H_1}\frac{\partial\rho}{\partial x}\,dz + \int_{-H_1}^{z}\frac{\partial\rho}{\partial x}\,dz\right]dx. \tag{9}$$

As seen from the mean hydrographic Yermak Section (Figure 6), the density lines below H_1 (YP2) are close to horizontal ($\frac{\partial\rho}{\partial x} \approx 0$) down to the sea floor where it can vary in time as seen in the time series from the YP moorings (Figure 10). Hence, the first term on the right hand side in Equation 9 becomes approximately equal to the bottom density term in Equation 7, which indicates that the bottom density term ($\overline{v_{b\rho}}$) contributes nothing to the total water column transport (see Morison, 1991 for an alternative derivation). Whatever $\overline{v_{b\rho}}$ adds to the bottom velocity is subtracted from the thermal wind velocity (first term in Equation 9). In conclusion, the averaged geostrophic velocity across the Yermak Section between YP3 and YP2, proportional to the Yermak Section volume transport, is therefore the baroclinic velocity, $\overline{v_t}$, integrated from the YP2 depth to the sea surface, plus the bottom pressure difference variability ($\overline{v_{dP}}$). If the flow is barotropic, that is, $\frac{\partial\rho}{\partial x}$ is zero, the bottom velocity ($\overline{v_{dP}}$) is the barotropic velocity and accounts for all the flow. . Hence, OBP recorders are excellent sensors when studying across-section barotropic geostrophic transport variability due to the dynamic effects of a changing sea surface from wind driven surface water transport, that is, air-ocean interaction processes.

3.3. Calculating Volume Transport and Anomaly of Along-Slope Heat Flux

We calculate volume transports across the Yermak Section by using the along-section averaged geostrophic velocity, that is, the along-section averaged of Equation 3, between YP3 and YP2 for the SB and between YP2 and YP1 for the SPC (Figure 8). Moreover, we assume constant water density and a barotropic flow so that the geostrophic bottom velocity, $\overline{v_b} = v_0 + \overline{v_b'}$, accounts for the total transport through the Yermak Section. As will be shown later, this assumption may hold for the winter months December–April, but is a crude assumption during summer and autumn when the water column over the YP is more stratified. Hence, we estimate the barotropic volume transport,

$$VT = A_{(SB,SPC)}\overline{v_b} = A_{(SB,SPC)}(\overline{v_b'} + v_0), \tag{10}$$
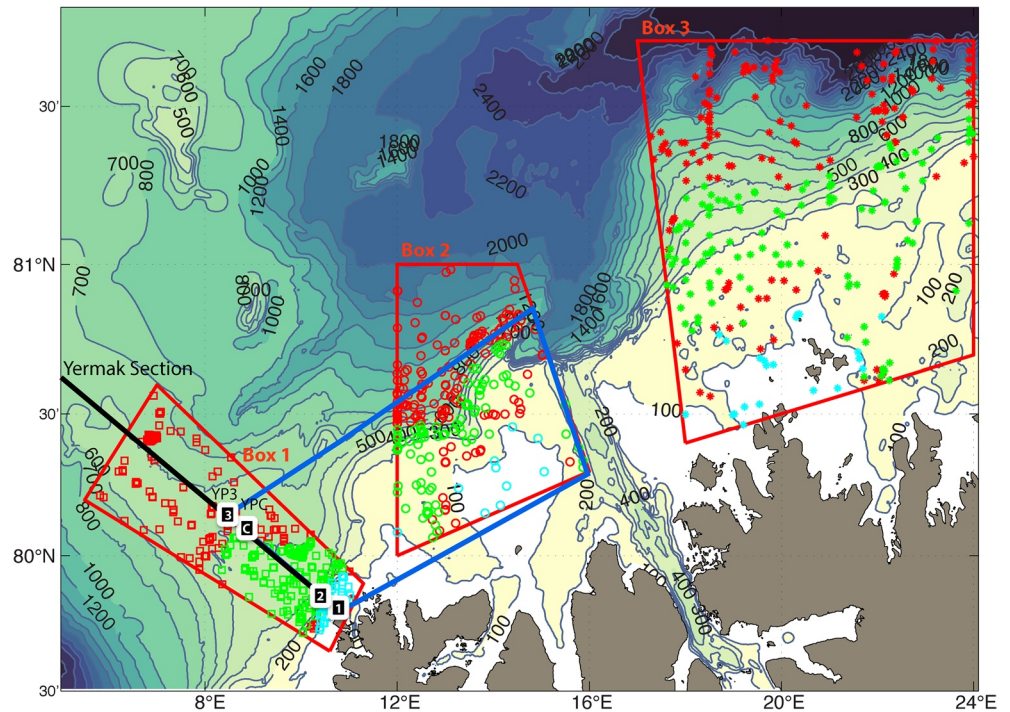
Figure 8. Bathymetric chart over the southwestern Yermak Plateau and the ocean area north of Svalbard including the Yermak Section (black line), the four REOCIRC moorings (YP1, YP2, YPC, and YP3), the study area for which the reference temperature T_m is estimated (blue box), and the three boxes where the monthly mean temperatures and a cooling parameter are calculated from historical data (red boxes). Within the red boxes, the cyan markers show the hydrographic data for the Spitsbergen Polar Current, the green markers the data for the SB, and the red markers the data that are not used in the monthly mean temperature calculations.

from our OBP time series (given by $\overline{v'_b} = \overline{v_{dP}}$ in Equation 7) and the mean surface current (v_0 from MDT data) since we focus on wind driven velocity variability. Moreover, a wind stress effectively changes the sea surface slope that drives the barotropic flow. $A_{(SB,SPC)}$ is the area of the SB and the SPC domain in the Yermak Section given by the distance between YP3 and YP2 (58.6 km) and between YP2 and YP1 (6.7 km), multiplied by the averaged water depths between these, 450 m depth and 75 m depth, respectively. Absolute barotropic transports are calculated for the SB since the mean surface current (v_0) can be estimated for the SB from satellite data, while only the barotropic transport variability can be calculated for the SPC.

For individual sections where the volume transport is not balanced, like the Yermak Section, heat transport is not well defined (Schauer & Beszczynska-Möller, 2009). However, a temperature flux or a relative heat flux can be calculated by using a reference temperature from the area of influence, which in our case is the sea north of Svalbard. Because we are concerned with the heat flux that actually alters the heat content north of Svalbard, we use a monthly climatological volume-averaged temperature for this region as a reference temperature T_m, following the approach of Lee et al. (2004). The ocean volume D north of Svalbard is called the domain and is within the blue box in Figure 8. The center of the volume north of Svalbard is here defined to be approximately 100 km downstream of the Yermak Section, and the actual volume D for the SB heat flux is restricted by the bottom depth between the 110 m (YP2) and 550 m (YP3) isobaths between 12°E and 16°E, and thus, representing the downstream SB domain east of the Yermak Section (inside the blue box in Figure 8). A similar domain over areas shallower than 110 m depth is defined for the SPC within the blue box. As explained in Lee et al. (2004), a heat flux across a surface interface A of the volume D can change the domain's average temperature if, and only if, the interface temperature is different from that of the domain's average T_m. Therefore we define a temperature flux relative to the domain's average temperature, which does not require a zero net mass flux across the section A (Lee et al., 2004), $\int_A (\vec{v}_g \cdot \vec{n})(T - T_m)dS$, where A is the cross-section area of the Yermak Section covering the SB of volume D, $\vec{n}$ is the normal vector of the area A,

$\vec{v}_g$ is the SB geostrophic velocity in the Yermak Section, T is the SB temperature at the interface A, and T_m is the volume-averaged temperature of the domain D north of Svalbard.

T_m is estimated in Section 4.1 using the 2-year temperature time series from the YPC mooring and historic hydrography data between 1993 and 2019 (Skogseth et al., 2019). First, we calculate the monthly mean temperature time series representative for each current in the Yermak Section using the depth-weighted temperature average from the bottom hydrographic time series at YP1 and YP2 for the SPC, and using the depth-weighted temperature average from the current meter mooring at YPC for the SB. Then we use these time series to calculate the 2-year monthly mean temperatures. Using the 2-year monthly mean temperatures, we then construct a linearly interpolated time series (1-h resolution) representing both years. Next, we would like to adjust this monthly mean temperature time series with a downstream cooling parameters/ temperature gradient so that it represents the T_m temperature for the domain within the blue box in Figure 8. To find this cooling parameter, a volume-weighted monthly climatological mean temperature is calculated from the UNIS Hydrographic Database over the period 1993–2019 (for months containing enough data) in three boxes representing the SPC (restricted by the 10–110 m isobath) and the SB (restricted by the 110–550 m isobath) domains north of Svalbard (Figure 8), while excluding the deep troughs indenting the shelf region. Climatological temperatures for the three boxes and the temperature gradients between the boxes are presented in Section 4.1.

As for the volume transport, we calculate only the heat flux contribution from the barotropic flow variability, and hence, the velocity in the temperature flux formulation becomes $\vec{v}_g \cdot \vec{n} = \overline{v_b} = \overline{v_b'} + v_0$. The barotropic heat flux contribution through an interface A is estimated from the formula

$$HF = \rho c_p A_{(SB,SPC)} \overline{v_b}(T - T_m) = \rho c_p A_{(SB,SPC)}(\overline{v_b'} + v_0)(T - T_m), \tag{11}$$

for both the SB and the SPC, where $A_{(SB,SPC)}$ is identical to the partial Yermak Section areas as for the volume transport formula in Equation 10, ρ is the sea water density, and $c_p = 4186$ JkgK^{-1} is the specific heat of sea water. Note that Equation 11 is not a heat transport, but rather the heat flux contribution from the barotropic flow variability in the SB and SPC toward the domain north of Svalbard.

4. Results and Discussion

4.1. Hydrographic Structure and Variability on the Yermak Plateau and North of Svalbard

In Figure 9, the time evolution of temperature, salinity, potential density, and buoyancy frequency from the YPC mooring are plotted in a Hovmöller diagram. The surface stratification with warm and less saline water in the upper layer is most distinct from June through December. The highest recorded temperature was 6.9°C in the surface layer (50 m depth) during September 2015. In October, the surface layer started to cool, while the temperature continued to rise in the deeper layers. As a result, the depth-averaged temperature peaked in November in both years. The temperature in the upper 400 m was warmer than 3°C during most of the measuring period, with the exceptions of March 2015 and early May 2016. The most saline water is located around 200 m depth and peaked at 35.15 in October 2014. Overall, the salinity was mostly above 34.9 in the entire water column during the 2 years. The exceptions are episodes with fresher water both in the surface and bottom layers, with the most pronounced freshening of the surface layer in November 2015. However, in 2016, the bottom layer became slightly fresher than 34.9. Winter stratification was weak and coincided with a stronger current (Figures 9c and 9d).

The temperature-salinity (TS) time series at the sea floor at YP1 (Figures 10a and 10b), YP2 (Figures 10c and 10d), and YP3 (Figures 10e and 10f) show that the TS-properties at the deepest level (Figures 10a, 10c and 10e), and thus the density anomaly, have large fluctuations particularly in wintertime. Although these are recorded near the sea floor at their respective locations, these three time series represent three different layers of the YP water column; the surface layer (YP1), the intermediate layer (YP2), and the bottom layer (YP3). Figures 10b, 10d and 10f show that the water masses fluctuate mostly between the two source waters, AW and Arctic Intermediate Water (AIW), but fresher Arctic Water (ArW) is also a source water at YP1, which is situated in the SPC.
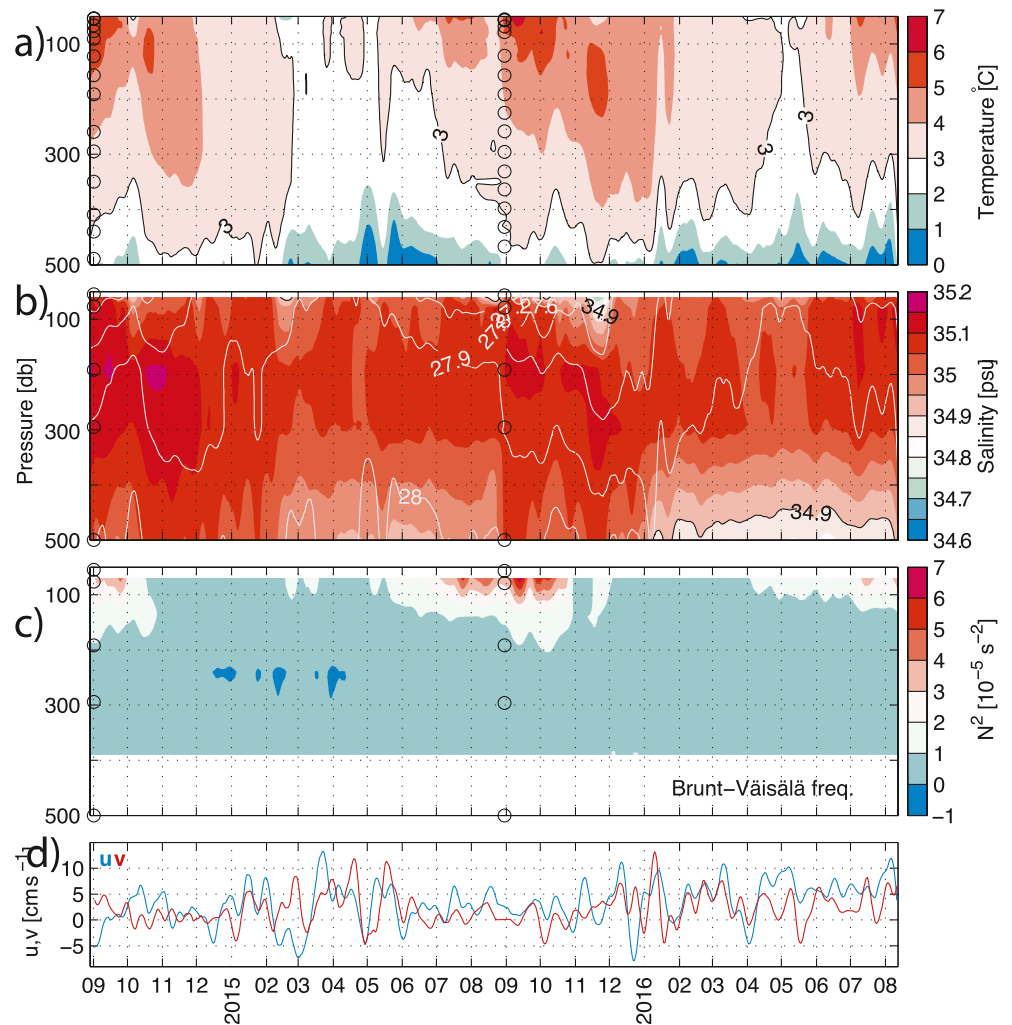
Figure 9. The hydrographic properties in the water column at YPC from August 28, 2014 to August 11, 2016 displayed in Hovmöller diagrams with time along the *x*-axis. (a) Temperature, (b) Salinity and potential density, σ_θ (gray lines), and (c) The buoyancy frequency N^2. The depths of the instruments are marked with black circles along the *y*-axis. The conductivity measurement at 500 m is adapted from YP3. (d) The depth-averaged current is calculated from the current meters at 60 and 500 m depth. The data are daily means smoothed with a seven days low-pass filter. Following the characteristics of Atlantic Water (AW) by Swift and Aagaard ([1981](#)), temperature above 3°C and salinity exceeding 34.9 have been outlined with black contours.

To estimate heat fluxes, we utilize all mooring temperature data and the UNIS Hydrographic Database (Skogseth et al., [2019](#)) for historic data to construct temperature time series representative for the YP and the domain north for Svalbard (Figure [8](#)), as described in the method section. The climatological temperatures for Box 1 (squares), Box 2 (circles), and Box 3 (stars) in Figure [8](#) are shown in Figure [11](#), and are found to support the seasonal signal variation by the 2-year YPC mooring. Error bars given by the standard deviation are added to the climatological temperatures from Box 1 (squares) on the YP for better comparison with the 2-year monthly mean temperatures from the YPC mooring. Downstream hydrographic data for the SPC domain (from 110 m depth and shallower onto the shelf) are sparser due to the chosen box domains. However, the summer and autumn months, July–October, can be used to estimate the temperature gradient from Box 1 (YP) to Box 2 while a winter month temperature difference (January) can be used for the Box2 to Box 3 temperature gradient estimate, in addition to the July–September months. For the SB (Figure [11b](#)), 8 of 12 months can be used to estimate a temperature gradient between Box 1 and Box 2. On the YP (squares), colder climatological winter temperatures are found in the SB domain (March–April) than the mooring
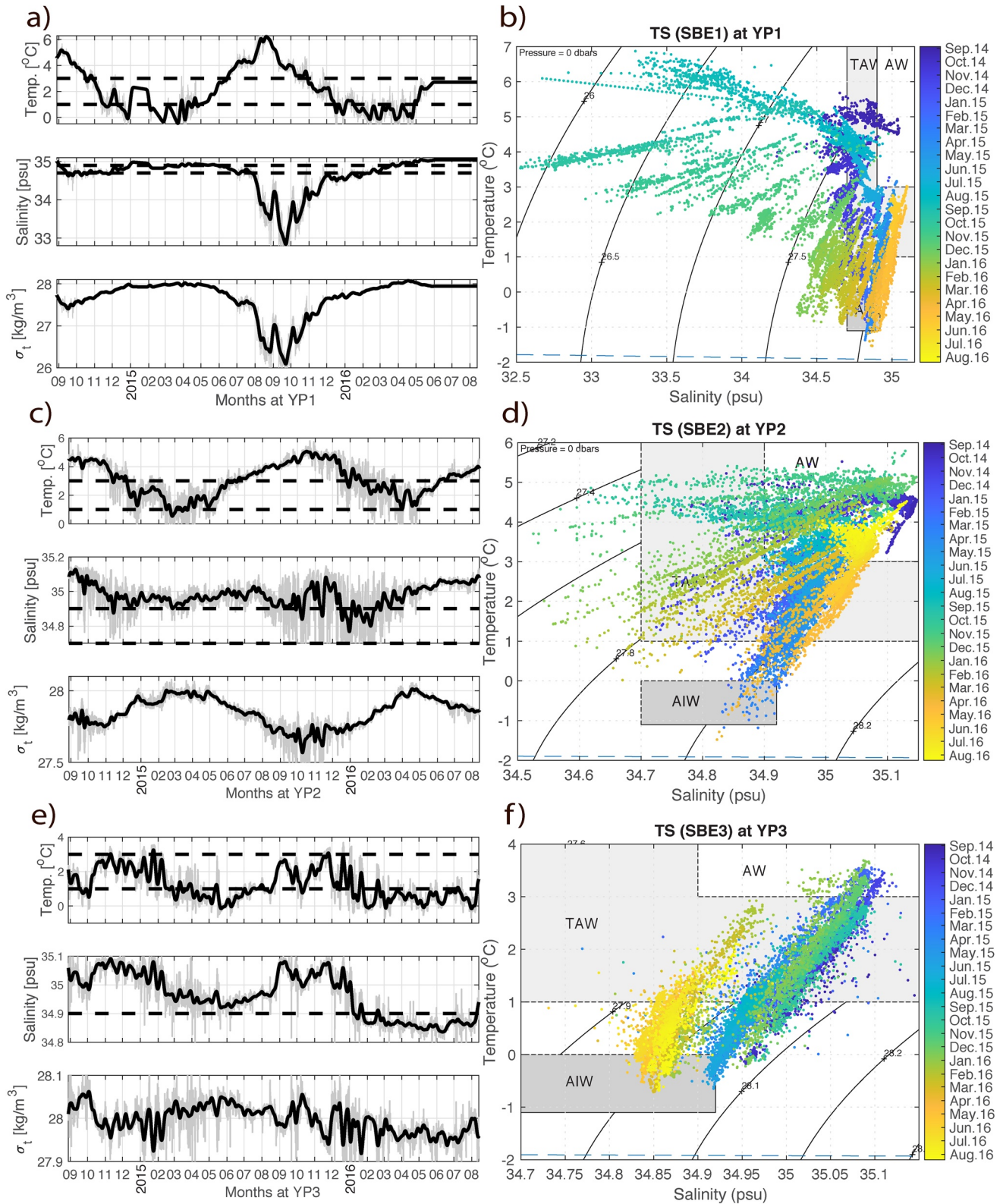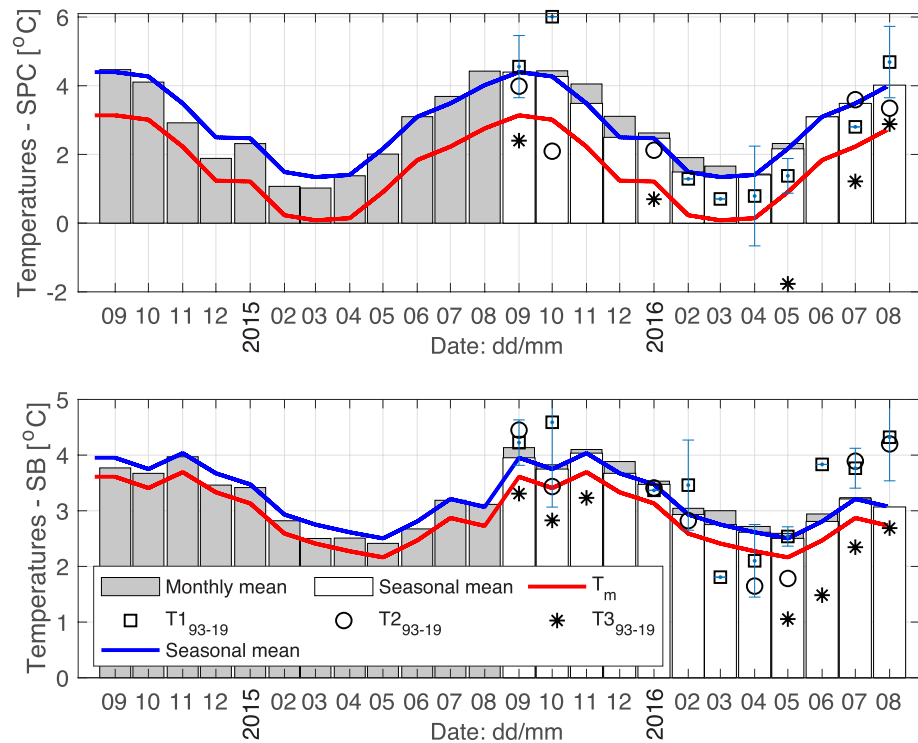
Figure 10.

Figure 11. Monthly mean temperature (gray bars) from the depth-weighted temperature time series at the YPC mooring. The 2-year monthly mean (white bars) is the 2 year average, while the blue line is 1-h linearly interpolated time series (matching the 1-h observations) based on the 2-year monthly mean values. This time series (blue line) is adjusted by the northward cooling gradient (Table 3) of (a) 1.26°C/100 km for the SPC and (b) 0.34°C/100 km for the SB to become the T_m (red line) used in our heat flux calculations. For comparison, climatological volume mean temperatures are shown for Box 1 ($T1_{93-19}$, southwestern Yermak Plateau), for Box 2 ($T2_{93-19}$, 12°E–16°E) and Box 3 ($T3_{93-19}$, 18°E–24°E) north of Svalbard in the SPC domain (110 m and shallower) and the SB domain (550–110 m depth). See Figure 8 for box illustrations and data availability.

data, while the summer and autumn temperatures are higher. Temperature gradients/cooling parameters between the different boxes in Figure 8, and for the different current domains, are given in Table 3.

The standard deviation (Table 3) is relatively large (when compared to the climatological mean) for both the current domains between the YP and Box 2, which could reflect the large variability on the YP since Box 1 is on a wide plateau while Box 2 follows a narrow slope area, although all hydrographic profiles represent the same depth range. The standard deviation reduces when both boxes follow the same slope and shelf area, as for Box 2 and Box 3. An increased cooling rate and temperature gradient are found for both current domains when we follow the currents downstream, which is expected since the currents flow into areas with colder water masses and that the air-ocean heat fluxes can increase while flowing into the area north of Svalbard (the Whalers Bay) in years with a reduced sea ice cover. Hence, we assume that heat loss to the atmosphere, vertical mixing, and heat loss through lateral mixing with the surrounding water masses are included in the cooling parameters in Table 3. These temperature gradients north of Svalbard are significantly larger than found in the hydrographic snapshot reported by Cokelet et al. (2008) (−0.25°C/100 km in the SB) and the gradients found by Saloranta and Haugan (2004) over the continental shelf and slope areas along western Spitsbergen. Therefore, we use the cooling rates estimated in Table 3 and construct the volume-averaged temperature, T_m, for the SPC and the SB domain (red lines in Figure 11) north of Svalbard by adjusting the

Figure 10. The measured temperature (T), salinity (S), and calculated density (σ_t) time series at (a and b) YP1, (c and d) YP2, and (e and f) YP3 presented as time series in (a), (c), and (e), including temperature (3°C and 1°C) and salinity (34.9) limits (dashed lines) for the definition of Atlantic Water. The same time series are plotted in TS diagrams in (b), (d), and (f), respectively, including constant density lines referred to the ocean surface. Water mass definitions (Table 2) are represented by gray boxes; Atlantic Water (AW), Transformed Atlantic Water (TAW), and Arctic Intermediate Water (AIW). The development in time is represented by the colorbar to the right.

Table 3
Temperature Gradients/Cooling Parameters Between the Boxes in Figure 8 Using Data From the UNIS Hydrographic Database (Skogseth et al., 2019) Between 1993 and 2019

Current domain	Box2–Box1 ($°C$/100 km)	Box3–Box2 ($°C$/100 km)
SPC[a]	-1.3 ± 0.6	-1.5 ± 0.2
SB[b]	-0.3 ± 0.1	-1.2 ± 0.1

[a]Spitsbergen Polar Current (SPC). [b]Svalbard Branch (SB).

2-year monthly mean temperature (blue lines in Figure 11) with the cooling rates from Table 3 (Box 2–Box 1 temperature gradient). We acknowledge the uncertainty in the T_m time series and the resulting standard deviation in the along-slope temperature gradients (Table 3). Care must be taken when calculating heat fluxes, however, valuable information on the northward heat flux variability can be found by using the formulation by Lee et al. (2004) when combining the constructed T_m times series with the observed barotropic flow variability.

4.2. The Spitsbergen Polar Current

The variability of the SPC is given by the bottom velocity anomaly $\overline{v'_b}$ in Equation 7 for the distance between YP1 and YP2, as shown in Figure 12 (black). This bottom velocity is the velocity anomaly calculated from the in-situ pressure difference ($\overline{v_{dP}}$, dark blue) and adjusted by the density variation in the water column between them ($\overline{v_{b\rho}}$, light blue). The latter component represents a seasonal variability determined by the YP vertical stratification (variability) and water masses being advected through the Yermak Section (baroclinic time scale), while the in-situ pressure difference consists of short-term variability controlled by the surface tilt (barotropic time scale). A negative $\overline{v_{b\rho}}$ between August and November 2015 is a result of a negative density anomaly along the sloping bottom between YP1 and YP2. Moreover, a strong negative density anomaly is evident at YP1 (Figure 10a) in autumn 2015, probably due to a higher air temperature than normal (August 2015 revealed a new monthly temperature record in Ny-Ålesund) and following river discharge and larger than normal freshwater input (Figure 10a) through strong precipitation events (September 2015) over Svalbard (met.no). A dampened and delayed version of the freshwater signal is seen at YP2 (Figure 10b) at the shelf break. Since the positive
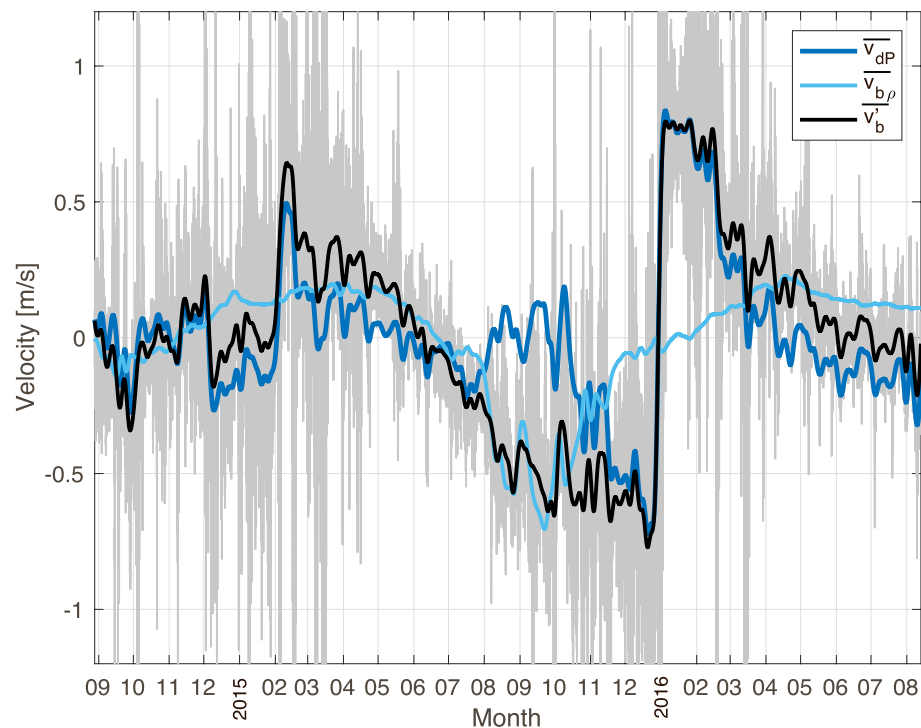

Figure 12. The bottom velocity anomaly $\overline{v'_b}$ (black) from Equation 7 for the distance between YP1 and YP2 as a sum of the velocity calculated from the bottom pressure difference $\overline{v_{dP}}$ (dark blue) and the velocity correction term $\overline{v_{b\rho}}$ (light blue) calculated from the bottom density difference between YP1 and YP2 and the difference in water column thickness between those. The gray curve/shading shows the hourly values for the $\overline{v'_b}$, while the black curve is the 1 week smoothed signal.

vertical velocity shear is controlled by onshore negative density gradients (downward sloping isopycnals in summer in Figure 6), the negative velocity anomaly $\overline{v_{b\rho}}$ at the sea floor signifies an increased vertical velocity shear and a strengthened baroclinic velocity component. Hence, the negative velocity anomaly $\overline{v_b'}$ at the sea floor between August and November 2015 is the sum of a larger positive vertical velocity shear, that is, a negative $\overline{v_{b\rho}}$, and a slightly positive pressure difference term, $\overline{v_{dP}}$, since the sea surface tilt is close to its mean value.

After November 2015, when the $\overline{v_{b\rho}}$ is reduced, a strong negative anomaly in $\overline{v_b'}$ is followed by a strong positive anomaly ($\overline{v_b'} \sim 75\ \text{cm s}^{-1}$) in late December 2015. As will become clear in Section 4.4, these strong anomalies are linked to the shift in wind stress directions and wind stress curl fields on the YP changing the sea surface elevation due to divergence or convergence of surface water along the coast, detected by the OBP recorders in $\overline{v_{dP}}$. In the wake of strong cyclone passages in DJF, the $\overline{v_b'}$ is reduced and the $\overline{v_{b\rho}}$ is increasing toward April/May in both years (Figure 12). Hydrographic time series close to the sea floor (Figure 10) shows an increasing density during this time period due to decreasing temperatures and relatively high salinities at YP1 and YP2. This might indicate cooling of AW on the shelf during winter time, which becomes the most dense water mass on the WSS due to its high salinity. Signature of this transformed AW is also seen in the Yermak Section for the winters between 2006 and 2018 (not shown), and the resulting isopycnals are tilting upwards toward the coast. The seafloor hydrographic time series at YP2 and YP1 respond with a positive density anomaly and give a positive bottom density velocity anomaly $\overline{v_{b\rho}}$. Therefore, we postulate that the positive bottom density velocity anomaly signifies the strength of the northward-flowing winter-cooled AW close to the bottom (F. Nilsen et al., 2016) and the baroclinicity of the water column on a monthly timescale. In addition, the wind stress curl drives the velocity variability on a much shorter time scale, on the order from f^{-1} to days.

4.3. The Svalbard Branch

Figure 13 shows the spatially averaged bottom velocity anomaly, $\overline{v_b'}$, based on the in-situ pressure difference and density anomaly between YP2 and YP3. The velocity is an average over the Yermak Section and contains different branches and dynamics across the YP that will be explained in the following. The 1-week smoothed velocity anomaly (black) shows a seasonal signal with the strongest positive current anomaly during winter from October to May. Moreover, the large variability in the raw data (gray shading) will be linked to wind forcing in subsequent sections.

A positive $\overline{v_{b\rho}}$ between February and July 2015 (light blue, Figure 13) is a result of a positive density anomaly along the sloping bottom between YP2 and YP3. As seen in Figure 10, the sea-floor hydrographic time series is close to its maximum density value during the winter months of this period, and nearly equal at all locations (YP1–YP3). Moreover, as shown by Figure 9, the large density anomaly at the bottom and increased bottom density velocity, $\overline{v_{b\rho}}$, occur when the water column on the YP is less stratified and close to homogeneous. This seems to happen suddenly in time as indicated by temperature and salinity in Figures 9 and 10. A similar sudden change in water mass properties (toward AIW at the bottom) and stratification (less stratified) started in January 2016. The latter does not show up as a strong anomaly in $\overline{v_{b\rho}}$ (Figure 13) since the bottom density anomalies at YP3 and YP2 adds up to approximately zero due to a lower salinity, especially at YP3. Prior to February 2015 and January 2016, $\overline{v_{b\rho}}$ is oscillating. This is also seen in the hydrographic time series and TS diagrams at YP3 (Figure 10), alternating between denser (cold and less saline) AIW and lighter (warm and saline) AW. A possible explanation to the oscillation involves the Arctic Front west of YP3 on the YP, between the AIW to the west and AW in the SB, clearly visible in the climatological summer section (Figure 6). These oscillations terminate when the water column converts permanently to a less stratified water column with AIW at the bottom, both in February 2015 and January 2016.

4.4. Ocean Current Variability Due to Atmospheric Forcing

The oscillating wind stress curl forcing can move density layers up and down in the water column (Ekman pumping). Moreover, in an Ekman pumping downwelling event, created by a negative wind stress curl forcing, the surface water is convergent and a positive surface level anomaly is created which changes the
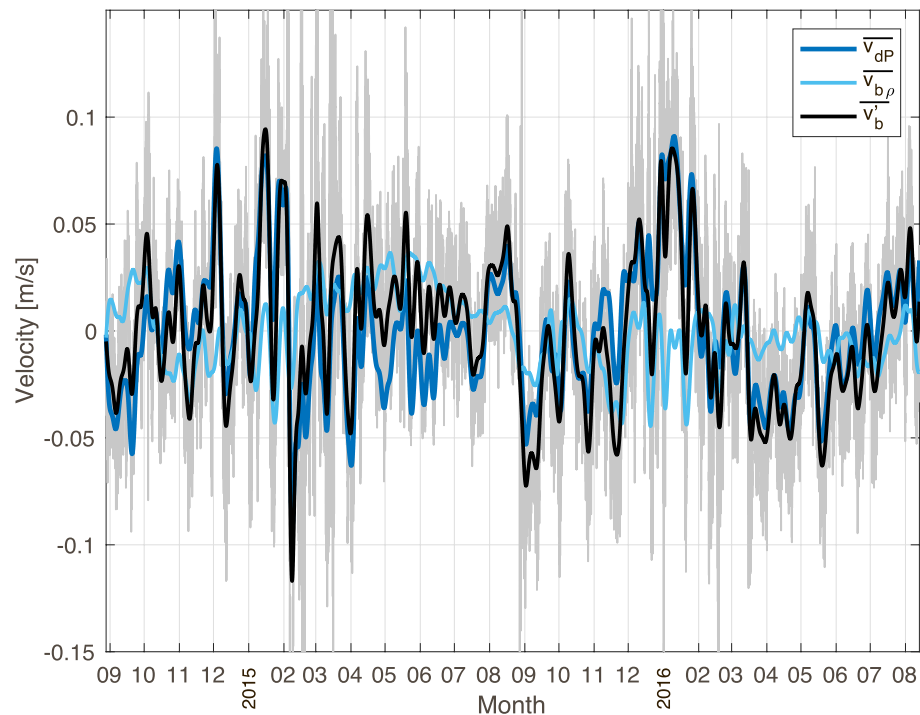
Figure 13. Same as Figure 12 but with the bottom velocity anomaly, $\overline{v_b'}$, (black) for the distance between YP2 and YP3.

surface pressure gradients and geostrophic flow anomalies. A wind stress along a coastline produces similar effects, and since the SPC follows the coast, we consider coastal upwelling (downwelling) with divergence (convergence) of surface water along the coast to be the main driver of geostrophic flow anomalies in the SPC. Note that a southerly/northerly wind component close to the coast line (coastal downwelling/upwelling) will create a negative/positive wind stress curl on the YP (over YP1 and YP2). In the following, we may refer to the sign of wind stress curl although coastal upwelling (northerly wind) or downwelling (southerly wind) is the driving mechanism for the SPC. Furthermore, since we are interested in the bottom geostrophic flow anomalies on the YP, we will focus on the link between the wind-driven sea surface changes and the barotropic response in the water column.

A spectrum of the wind stress curl time series in Figure 4 is shown in Figure 14a. Broad and not significant peaks are shown for periods around 5 days, 1 week, and one and a half week which are typical time spans for the passage of low-pressure systems over Svalbard (Wickström et al., 2020). The same peaks show up in the coherence spectrum between the wind stress curl time series and the bottom geostrophic velocity anomaly $(\overline{v_b'})$ close to the coastline between YP1 and YP2 (close to the 95% confidence level in Figure 14b), that is, in the SPC, while the geostrophic flow variability between YP2 and YP3 shows no coherence with the wind stress curl (Figure 14b). Hence, as will be discussed later, the current close to the coastline has a strong link to the variability in surface elevation created by the wind stress component along the coast on the YP.

The annual mean wind stress field for 2015 (Figure 4) shows a prevailing northeasterly direction over the YP with a more southeasterly direction on the WSS. These mean directions signify both (a) cyclone pathways from the Nordic Seas into the Barents Sea, resulting in northeasterly wind stress north of Svalbard and (b) cyclone pathways traversing the Fram Strait toward the Arctic with more southerly component along the WSS. On the northwestern corner of Svalbard, scenario (a) results in a low-level tip jet with intensified wind stress over the YP, similar to the jet in the Hinlopen Strait and around South Cape as described by Sandvik and Furevik (2002) and Reeve and Kolstad (2011), respectively. Low-level tip jets occur in many locations where airflow converges around obstacles, such as islands. Along the coast of western Spitsbergen, southerly wind stress in scenario (b) results in Ekman transport of the surface Ekman layer toward the coast and a downwelling in the layers below (same response but with opposite sign for northerly winds). But more
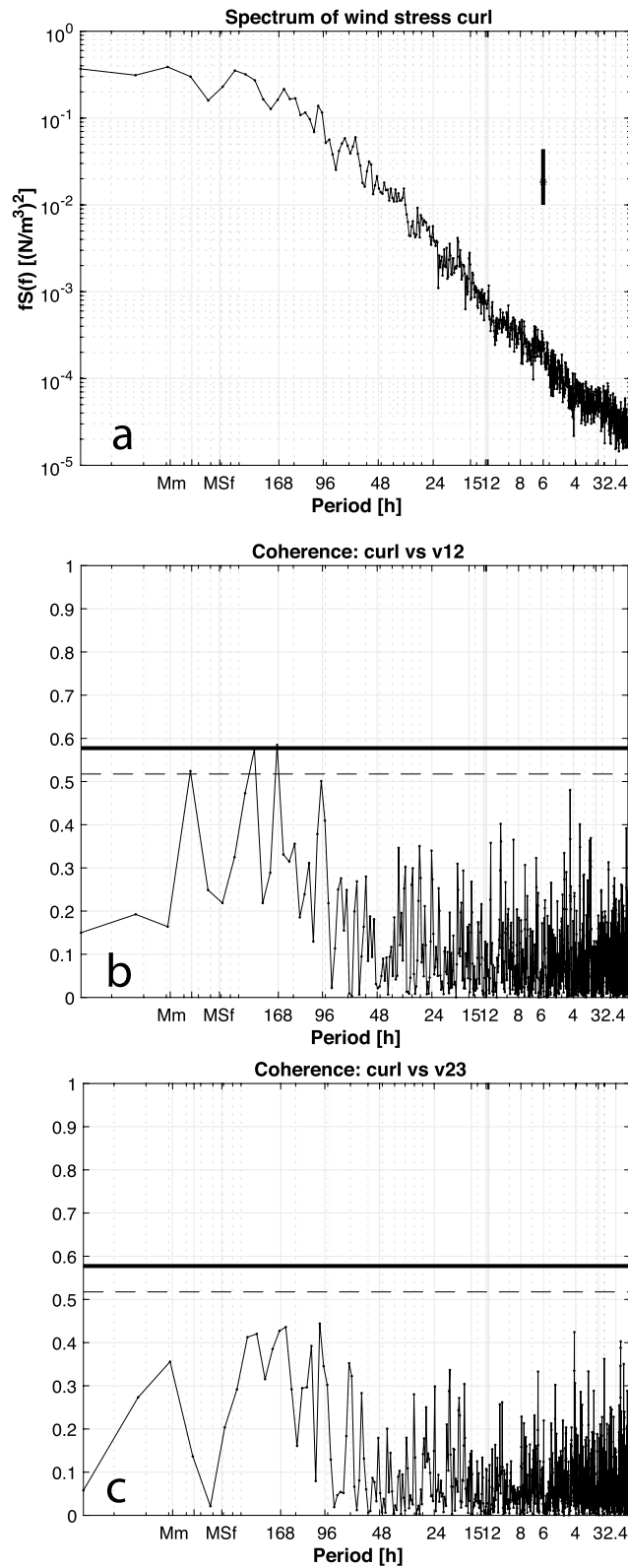
Figure 14.

importantly, this redistribution of surface water cause changes to the surface tilt and the barotropic pressure gradient. The mean wind stress curl over the YP is positive for 2015 (Figure 4), which is also the case for 2014 and 2016 but with smaller amplitudes (not shown). A positive wind stress curl and a northerly wind stress component close to the coast over the YP results in divergence of water in the surface Ekman layer and a decreasing sea surface level toward the coast, and thus, a negative anomaly to the barotropic velocity component on the YP.

To investigate the influence of the wind stress curl variability on the variability in the SPC and the SB, a lagged Pearson's correlation coefficient has been estimated between the wind stress curl field and the barotropic geostrophic current variability (2014–2016), $\overline{v_b'}$, between YP1 and YP2 (Figure 15a) and between YP2 and YP3 (Figure 15b), respectively. Both correlation coefficients (Figures 15a and 15b) are significant within the 95% confidence interval on the YP and along the WSS where the correlation coefficients (Figures 15a and 15b) have a time lag around 10 h. Hence, locally on the YP, the correlation signifies a geostrophic adjustment since the time lag is on the order of the inertial frequency f^{-1}, and the negative wind stress curl represents an increased SPC and SB due to convergence of surface water and an associated increased sea surface tilt toward the coast.

The correlation coefficient for the SPC (Figure 15a) has a minimum over the YP1 mooring close to the coast indicating a direct influence on the SPC when the sea surface tilt toward the coast is increased or reduced. This means a speeding up of the SPC when the wind stress curl is negative with an associated increased surface pressure gradient force or a slowing down of the SPC when the wind stress curl is positive with a decreased surface pressure gradient force, respectively. Upstream of the YP, along the western coastline of Spitsbergen, the correlation coefficient is also significant (95%) and represents an increase or decrease in the SPC due to a unified increase (negative wind stress curl) or decrease (positive wind stress curl) of the surface pressure gradient, respectively, along most of the West Spitsbergen coastline. Moreover, there is a strong correlation west of Forlandet complying with F. Nilsen et al. (2016), which showed that the SPC continues northward along the west coast of Forlandet after flowing along the northern side of the Isfjorden Trough and around the southern tip of Forlandet. Compositing all the wind stress curl fields for periods when the SPC is larger than 2 standard deviations from the mean, one finds that the average wind stress curl field (Figure 16a) supports a convergence of surface water toward the coast on the YP with dominating southerly winds along the WSS. There is also a negative curl close to the coastline that can speed up the SPC. To reduce the SPC at the YP, the wind stress has to be northeasterly north of Svalbard (Figure 16b). This northeasterly wind stress situation with a positive wind stress curl, diverges the surface water offshore, which reduces and potentially halts or reverses the SPC over the YP.

An extraordinary increase in the arctic surface air temperature (SAT) was observed in the winter season of 2015/16 after an extreme Atlantic windstorm entered the Nordic Seas in late December 2015 (Kim et al., 2017). This storm, which was named "Frank" by the U.K. Met Office, showed a minimum central pressure of 928 hPa on December 30, 2015. A long-term effect over the Eurasian Arctic sector was anomalous SAT prominent in the northern Barents and Kara Seas toward central Siberia, with a maximum local SAT increase of up to 23°C during the first 7 days of January 2016. The wind stress time series in Figure 4 captures "Frank" where the wind stress changes from northerly to southerly on December 28, and respectively, the wind stress curl changes from strongly positive to negative values over the YP. The response in the SPC (Figure 12) and the SB (Figure 13) is instant (within the geostrophic adjustment time frame) with the largest and most long-lived positive velocity anomaly (January and into February) in both the SPC and the SB in our 2-year time series. As will be shown later, these anomalies represent a large oceanic heat flux across the YP and toward the Eurasian Arctic, and the extreme windstorm that entered the Arctic Ocean was therefore a major factor for these positive anomalies in heat transport and sea ice loss (Kim et al., 2017).

Figure 14. (a) Power spectrum of the wind stress curl at the northwestern corner of Spitsbergen (green triangle in Figure 4) and (b) coherence spectra between the same curl time series and the calculated bottom geostrophic velocity anomaly ($\overline{v_b'}$) between YP1 and YP2 and (c) between YP2 and YP3. A Hanning window of 2048 h is used in the pwelch method with a 50% overlap. The 95% significance level in (a) is indicated by the black vertical line where the asterisk is placed on a peak value to see if the peak is above the noise level. The 95% and 90% significant levels are shown by a thick line and a dashed line in panels (b) and (c), respectively.
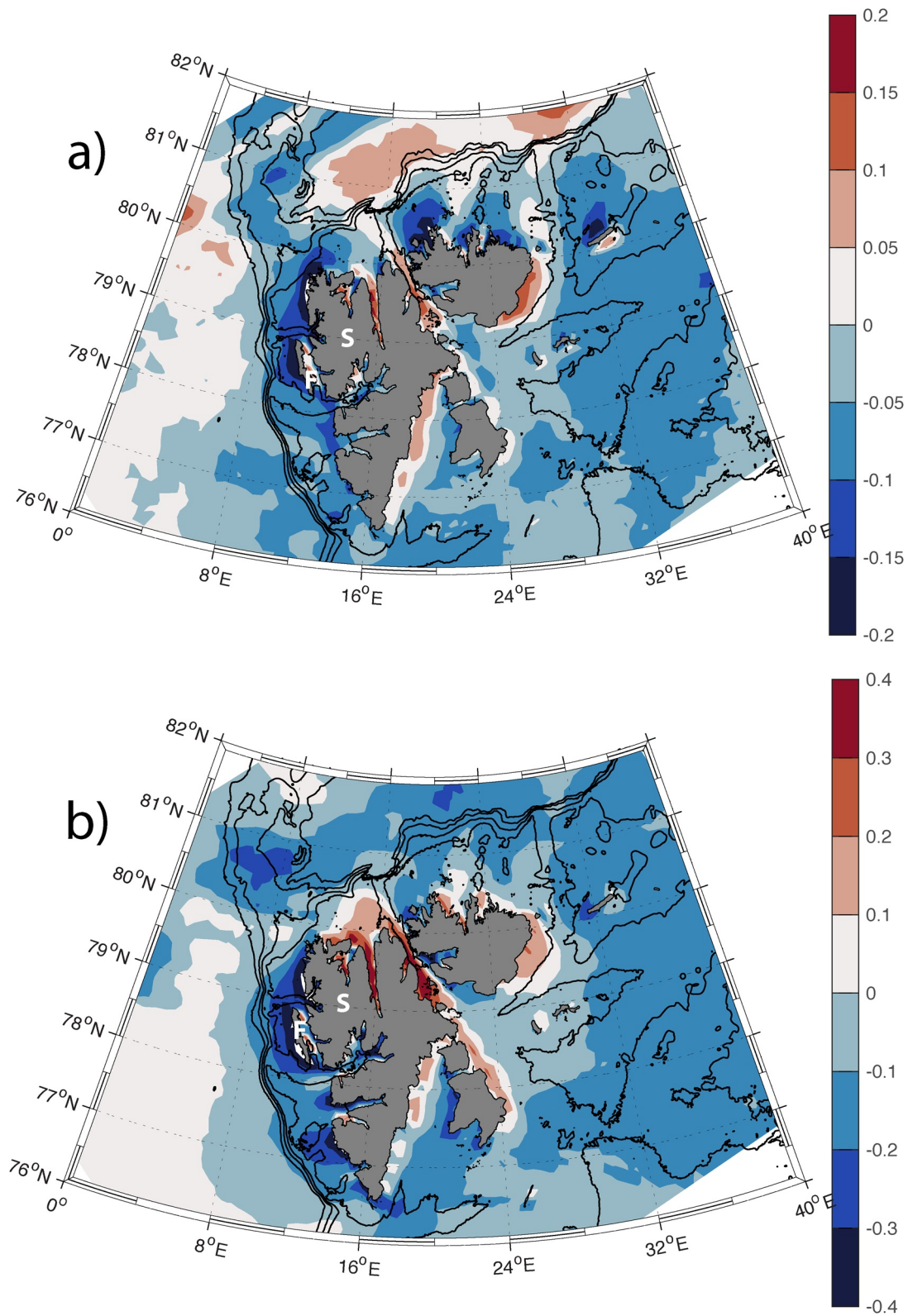
Figure 15. Wind stress curl field (calculated from NORA10 data) correlated (Pearson's correlation coefficient) with (a) The Spitsbergen Polar Current $\overline{v_{dP}}$ between YP1 and YP2, and (b) The same correlation with the SB $\overline{v_{dP}}$ between YP2 and YP3. The white F is Forlandet and the white S is Spitsbergen.
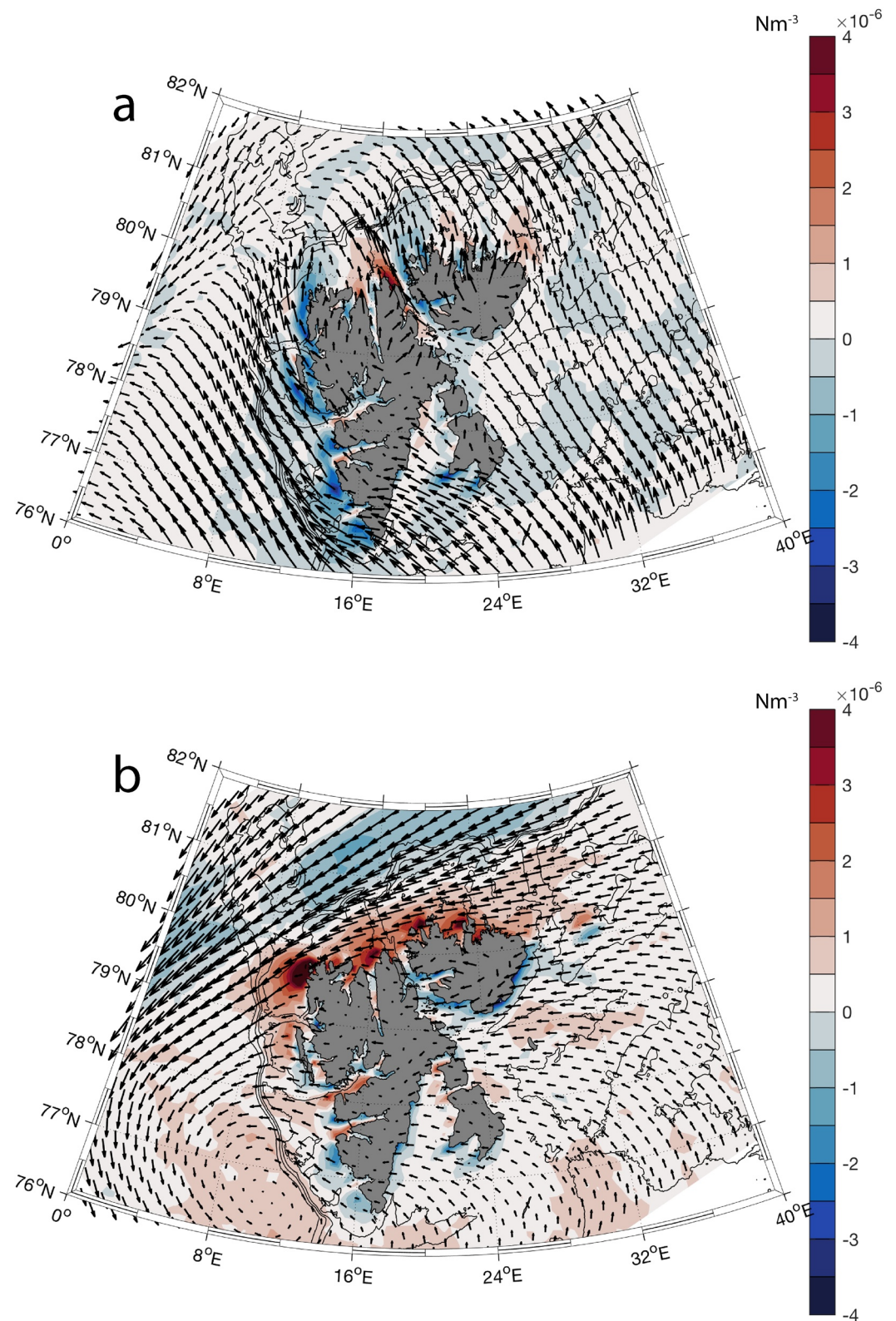
Figure 16. The average surface wind stress and wind stress curl field for all the cases when the Spitsbergen Polar Current (SPC) ($\overline{v_{dP}}$ between YP1 and YP2) is (a) >2 STD($\overline{v_{dP}}$) and (b) <−2 STD($\overline{v_{dP}}$), and thus, the largest directional variability in the SPC.

The correlation coefficient for the SB (Figure 15b) has a large negative value along the coast south of the YP, where the negative correlation extends toward the shelf break down to the southern tip of Forlandet. The wind stress and wind stress curl forcing make the barotropic slope-break branch of the WSC follow shallower isobaths (Crews et al., 2019; F. Nilsen et al., 2016) during negative wind stress curl, and the reverse effect during positive wind stress curl. Moreover, passages of strong cyclones in the Fram Strait pile up water along the WSS, which set up topographically guided currents along the shelf break and into the troughs indenting the WSS, while strong northeasterly winds due to cyclones situated in the Barents Sea can have the opposite effect. Hence, some of the AW in the barotropic WSC branch is forced to circulate in these troughs. This circulation is named the Spitsbergen Trough Current (STC; F. Nilsen et al., 2016) and represents a longer and slower route of AW toward the Arctic Ocean. The correlation coefficient for the SB over the WSS and between the troughs (Figure 15b) indicates that the STC contributes to the SB, most likely the part of the SB that is, confined to the slope closest to the coast on the YP. When the STC reach the YP it might be detected as a relatively high salinity water mass (close to the AW definition) between 200 and 100 m depth and close to the shelf break (found at 120 m depth), and with a temperature close to the AW temperature in the SB, but lower due to the longer flow path with larger accumulated heat loss on its way (F. Nilsen et al., 2016). This signature of the STC is seen in the climatological Yermak Section for the summers from 2006 to 2018 (Figure 6), where the isopycnals are tilting upwards toward the coast, both in winter (not shown) and summer.

Compositing all the wind stress curl fields for cases when the SB is >2 standard deviations from the mean, it is evident that the average wind stress curl field (Figure 17a) supports a convergence of surface water toward YP2 and divergence of surface water at YP3, increasing the surface tilt from YP3 toward YP2 and driving the SB on short time scales. Remember that the correlation time lag was on the order of f^{-1} and therefore correspond to the direct geostrophic adjustment on the YP due to an increased surface tilt. Figure 17a also confirms that a strong SB is linked to the wind stress and wind stress curl forcing upstream of the YP, speeding up the barotropic slope-break branch of the WSC and make it follow shallower isobaths. This is associated with the southerly wind along the WSS and cyclones close to Svalbard or in the Fram Strait. A reduced SB is associated with the northerly wind along the WSS and a positive wind stress curl on the YP (Figure 17b). Positive wind stress curl reduces the onshore surface tilt and the upstream positive wind stress curl is retarding the barotropic WSC branch, which is not a favorable setup for the STC.

4.5. Volume Transport and Heat Fluxes

The SB, the Yermak Pass Branch (YPB), and the Yermak Branch (YB) are the primary routes through which warm AW enters the Arctic Ocean. These branches either flow around (YB) or pass over (SB, YPB) the YP. Here, we will discuss the dynamics that control the overflow of AW in the SB and arctic type water in the SPC from direct measurements, calculate volume and heat fluxes, and link them to the most important driving forces.

4.5.1. Volume Transport

The SPC is a surface current along the west coast of Spitsbergen carrying arctic type water, and as it flows northward, the SPC visits fjord-mouth areas and accumulates freshwater along the west coast of Spitsbergen. An absolute transport across the Yermak Section is not known; however, the OBP measurements (Figure 18a) show a peak to peak variability of 0.8 Sv which is a high transport across this narrow passage (6.7 km). This large variability is mostly driven by wind stress variability over the YP, which controls the amount of colder and fresher water that enters the north of Svalbard. Finally, the WSS has been flooded with AW that makes the shelf water more Atlantic (Cottier et al., 2007; F. Nilsen et al., 2016; Skogseth et al., 2020; Tverberg et al., 2019), that is, warmer and saltier, which is also reflected in the hydrographic time series at YP1 (Figures 10a and 10b) and YP2 (Figures 10c and 10d). Hence, in recent years, the SPC might contribute to a positive heat flux and salt flux toward the ice-covered waters north of Svalbard.

From their model studies, both Koenig et al. (2017) and Crews et al. (2019) found that the YPB was winter-intensified and that the SB lacked seasonality with an average transport of 0.8 Sv. However, the importance of the seasonal variations in the SB is apparent from the resultant transports from in situ measurements as seen in Figure 18b. This time series is the volume transport variability around the average SB
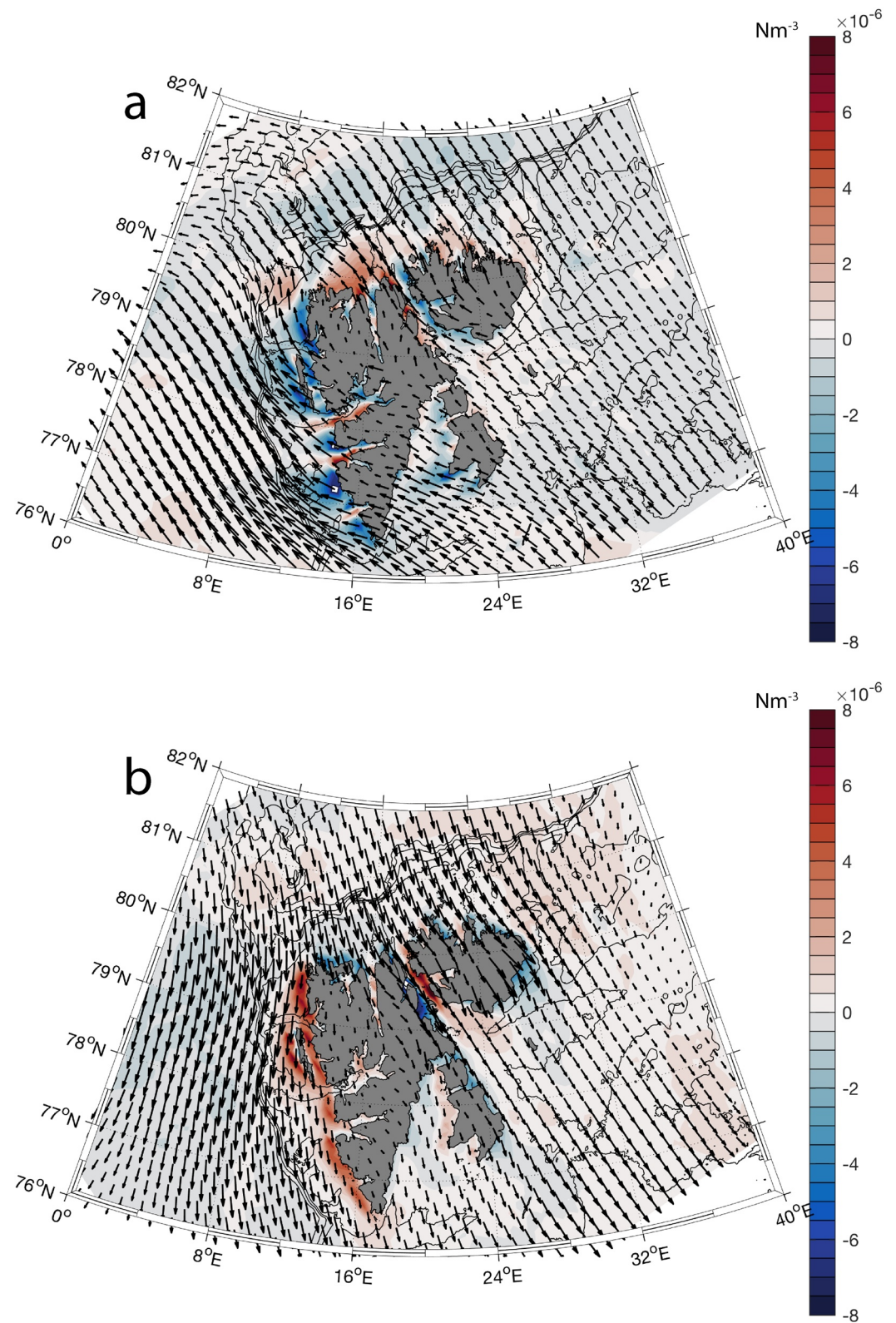
Figure 17. The average surface wind stress and wind stress curl field for all the cases when the Svalbard Branch (SB) ($\overline{v_{dP}}$ between YP2 and YP3) is (a) $>2\,\mathrm{STD}(\overline{v_{dP}})$ and (b) $<-2\,\mathrm{STD}(\overline{v_{dP}})$, and thus, the largest directional variability in the SB across the Yermak Plateau. Note the increased wind stress curl color scale compared to Figure 16.
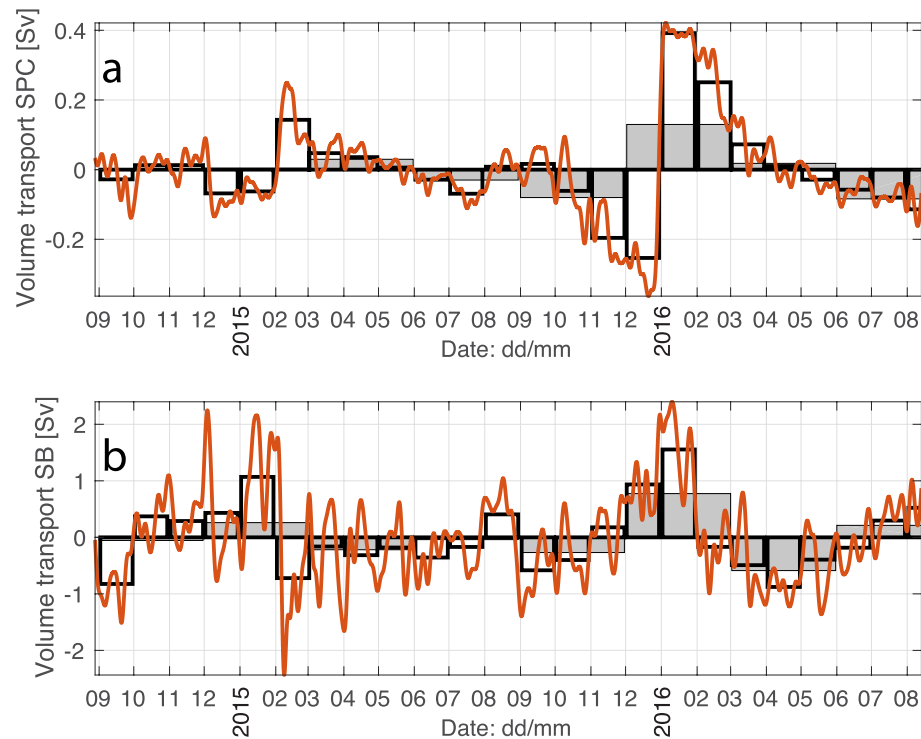
Figure 18. Volume transport anomaly (in Sverdrup, 1 Sv = 10^6 m^{3}s^{-1}) for the 1-week smoothed time series (red), monthly averages (black bars) and seasonal averages (DJF-MAM-JJA-SON) in (a) the Spitsbergen Polar Current (6.7 km wide and 75 m deep cross-section) and (b) the Svalbard Branch (58 km wide and 450 m deep cross-section).

transport of 1.1 Sv (Sv = 10^6 m^{3}s^{-1}), estimated from the MDT data presented in Figure 5. Hence, the peak to peak variability in the SB can exceed 4 Sv and the time series show a distinct seasonal variability with the highest transport in the DJF months, and an interannual variability between the 2 years. These seasonal and interannual variations were also reported by Morison (1991). Moreover, distinct seasonal variability and peak-to-peak transport variability are also in agreement with the upstream seasonal variability and peak-to-peak transports observed in the WSC barotropic branch from the long-term monitoring program at 78°50′N (Beszczynska-Möller et al., 2012), relatively close to the YP.

As described in Section 4.4, the response in the SPC (Figure 18a) and the SB (Figure 18b) is instant (within the time frame of geostrophic adjustment) to a changing wind stress and wind stress curl over the YP. This is apparent around New Year 2016 when an extreme Atlantic windstorm entered the Nordic Seas in late December 2015; the SPC had its largest positive volume transport anomaly of 0.4 Sv lasting for 1 month and the SB increased by approximately 1 Sv over the same period (to a total anomaly of 2 Sv). Moreover, this is also the time of the year (December–May) when long-period oscillations become significant on the YP as described in Ersdal (2020), with monthly and fortnightly oscillating signals overlying the wind-driven volume transport for the SB (Figure 18b). Hence, as illustrated in Figure 6b, it is meaningful to split up the SB variability into a slope-confined and directly wind-driven inner SB, and an outer SB for the flat part of the YP covered by the Yermak Section and driven by the long-period oscillations (Ersdal, 2020). The volume transport variability of the inner SB is controlled by the sign of the wind stress curl over the YP close to the northwestern corner of Spitsbergen and the outer SB volume transport variability might be dominated by long-period oscillation. The generating mechanisms for these long-period oscillations are beyond the scope of this study and will be studied in separate study. Moreover, a monthly average (Figure 18) balances these oscillations and, we are left with the dominating wind-driven volume transport variability.

4.5.2. Heat Flux

The heat flux anomaly estimates in the SPC and the SB are shown in Figures 19a and 19b, respectively, which are the $dT = T - T_m$ time series (red line) multiplied with the volume flux anomaly from Figure 18.
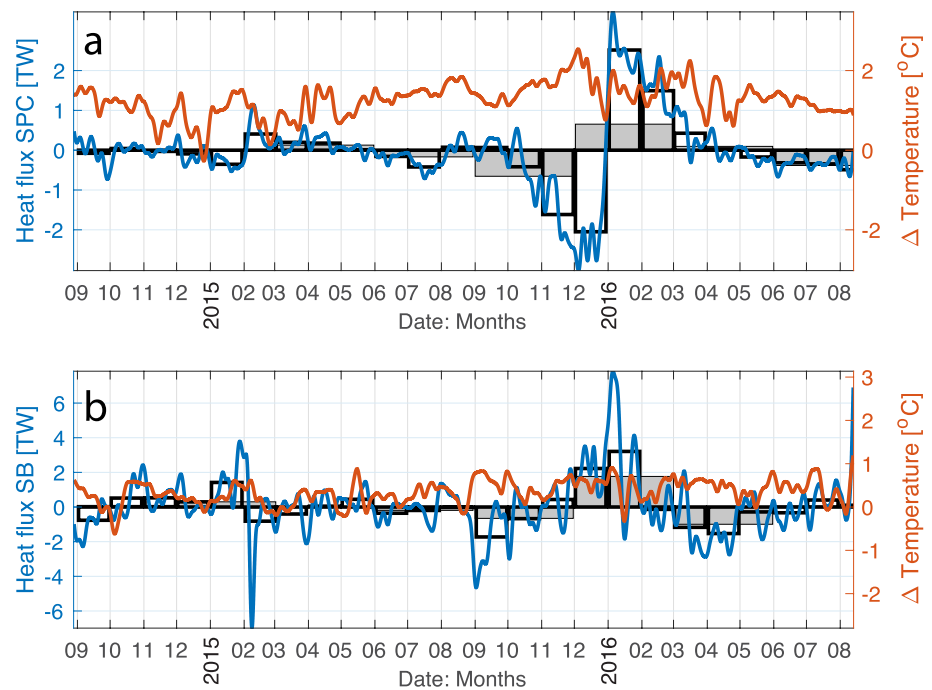
Figure 19. Heat flux anomaly (in TW = 10^{12} W) for the 1 week smoothed time series (blue), monthly averages (black bars), and seasonal averages (DJF-MAM-JJA-SON) in (a) The Spitsbergen Polar Current and (b) The Svalbard Branch. The temperature difference $(T - T_m)$ time series between the depth-weighted average on the Yermak Plateau and the northern domain volume-average temperature, T_m (Figure 11), for (a) The Spitsbergen Polar Current domain and (b) The Svalbard Branch domain.

The 1-week smoothed heat flux is plotted together with the monthly and seasonal (DFJ-MAM-JJA-SON) heat flux averages. In winter, the heat flux anomalies toward the sea ice north of Svalbard can be over 3 TW in the SPC and over 6 TW in the SB due to strong short-time wind events. Moreover, the monthly mean heat flux anomaly can be over 2 TW for the SPC and around 2 TW for the SB. Although these heat flux anomalies are an order of magnitude smaller than the absolute heat flux toward the Arctic Ocean (Beszczynska-Möller et al., 2012), Onarheim et al. (2014) have shown that such anomalies can have a significant effect on the local sea ice cover and surface air temperature north of Svalbard. For instance, if an extra amount of heat of 6 TW reaches the ice and is equally distributed over the study area north of Svalbard (83 × 82 km), a 1-m thick sea ice cover above the SB would melt in about 3 days. As noted by Onarheim et al. (2014) and shown by Polyakov (2017), only part of the excess heat flux will be used for sea ice melting and up to 50% of the warm anomalies can be advected farther eastward and into the Arctic Ocean boundary current. However, with a winter mean sea ice concentration of well below 50% in this area, an ice-free water may be reached faster. Hence, short-time (days), high-impact heat fluxes can keep the area above the SB ice-free during winter. Figure 9 shows that the SB has a warm surface signature throughout the year, available for sea ice melting. Furthermore, as seen in Figure 11a, the SPC does not reach the freezing point temperature during the winter months, and the large positive heat flux in the SPC (a surface current) will thus have a direct effect on the shelf and fjord sea ice north of Svalbard.

Figure 9 shows that the temperature in the water column on the YP was higher in winter 2015/16 than the winter 2014/15, which is also reflected in the temperature difference $dT = T - T_m$ for both the SPC and the SB (Figure 19). The heat flux anomalies in Figure 19 are mostly driven by the volume flux variability. However, since we are able to calculate a mean volume transport of 1.1 Sv for the SB, based on the MDT data, we can further calculate the barotropic heat flux in the SB that can alter the heat content north of Svalbard. It is therefore possible to evaluate the heat flux contribution of a changing temperature signal in the SB (and thus in the barotropic WSC branch), advected by the mean flow toward the Arctic Ocean. In Figure 20, the total heat flux time series have been decomposed into four terms (Lee et al., 2004),
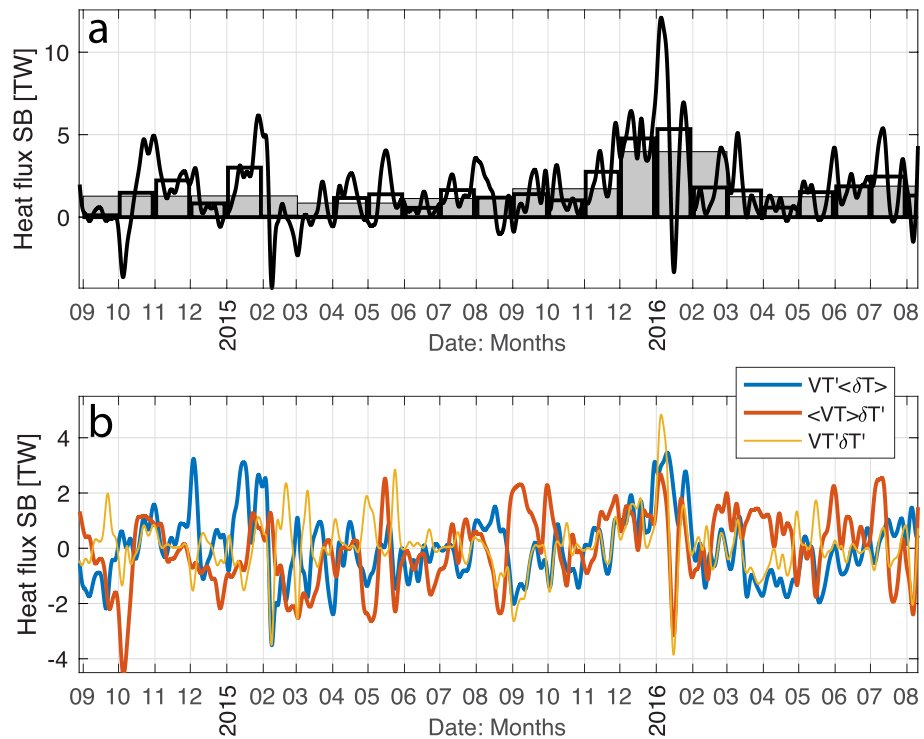
Figure 20. (a) The total heat flux (in TW = 10^{12} W) that alters the heat content north of Svalbard for the 1-week smoothed time series (black), monthly averages (black bars), and seasonal averages (DJF-MAM-JJA-SON) in the Svalbard Branch. (b) The heat flux is split into three anomaly components; the advection of mean temperature difference by anomalous flow (blue line), that is, the volume flux variability, the advection of anomalous temperature difference by mean flow (red line), and the advection of anomalous temperature difference by anomalous flow (yellow line).

$$\rho c_p A v_b (T - T_m) = \rho c_p A \left(\overline{v_b' \overline{\delta T}} + v_0 \delta T' + \overline{v_b' \delta T'} + v_0 \overline{\delta T} \right), \tag{12}$$

where ρ is the sea water density, $c_p = 4186$ JkgK^{-1} is the specific heat of sea water, $v_b = \overline{v_b'} + v_0$ is the OBP velocity anomaly $\overline{v_b'}$ plus the mean velocity $v_0 = 0.043$ ms^{-1} (from MDT data) for the entire section, and $dT = (T - T_m) = \overline{\delta T} + \delta T'$ split into an average temperature difference between the YP and the SB domain north of Svalbard ($\overline{\delta T} = 0.3°$C) and the deviation from this mean ($\delta T'$). The four terms in Equation 12 correspond to, respectively, the advection of mean temperature difference (Cokelet et al., 2008; Saloranta & Haugan, 2004) by anomalous flow (i.e., the volume flux variability), the advection of anomalous temperature difference by mean flow, the advection of anomalous temperature difference by anomalous flow (the oscillation term), and the advection of mean temperature difference by mean flow.

Except for a strong wind event in January–February 2015 facilitated by the $\overline{v_b' \overline{\delta T}}$ term controlled by the volume flux (blue line in Figure 20), the extra heat flux to northern Svalbard is small during the first winter (2014/15) with around 1 TW for the 3-month average. During the second winter (2015/16), the two terms with variable temperature difference, $\delta T'$, amplified the heat flux term controlled by the volume flux and made the interannual heat flux contrast larger. These interannual variations reveal a colder water mass, or a water mass close to T_m, flowing over the YP the first winter, while the water column had a positive temperature difference the second winter (2015/16), bringing more heat into the SB domain north of Svalbard than compared to the long-term average. Hence, the total heat flux of the SB is dependent on the water masses present in the Yermak Section and shows that the $v_0 \delta T'$ term can be linked to the increasing temperature trend observed in the WSC for the last decades (Hanssen-Bauer et al., 2019; Onarheim et al., 2014). However, an injection of warmer AW to the domain north of Svalbard on shorter time scales are facilitated by a

positive $\overline{v_b' \delta T}$ term, together with a positive $v_0 \delta T'$ term, which signify a speed up of the slope-confined inner SB (with warmer water than the domain average T_m) due to strong wind forcing events like in January–February 2015 and December–January 2015/16. Also note that the anomaly term, $\overline{v_b' \delta T'}$, has a large oscillating amplitude with a period from 14 days to 1 month with a large influence on the barotropic heat flux for the winter and spring months. Finally, for both spring periods in Figure 20, the MAM months result in smaller barotropic heat fluxes for the SB (around 1 TW) as compared to the DJF months, and this is when other branches across or around the YP (e.g., YPB and YB) becomes more important.

5. Summary and Concluding Remarks

The barotropic volume transport anomaly in the SPC and the SB, and their heat flux anomaly across the YP, are well represented by the three OBP moorings deployed in the Yermak Section from August 2014 to 2016. The peak-to-peak variability can exceed 0.8 Sv in the SPC, and 4 Sv in the SB, and the time series show a distinct seasonal variability with the highest transport in the DJF months, with an interannual variability between the two years. The average velocity anomalies estimated from OBP recorders across the Yermak Section are ideal for detecting the wind forced dynamics of the SPC and the SB, which is the dominating driving force for the shallow well-mixed YP where the warm AW has to cross over to reach the sea ice north of Svalbard. On the YP, the volume transport anomaly in the SPC and the SB is mostly driven by the horizontal change in the sea surface elevation, for example, the surface pressure gradient, while the stratification controls the velocity shear that can be strong in the SPC and week in the SB. This study has shown that it is a good correlation between the wind stress curl over the YP (and downstream on the WSS) and the barotropic volume transport anomaly in the SPC and the SB across the YP. The volume transport in the SB is largest during the DJF winter months due to the strength and trajectories of the winter storms, where cyclones entering Fram Strait or traversing Svalbard are favorable for a large positive volume transport anomaly in both the SPC and the SB. Adding the MDT transport estimate for the Yermak Section to the OBP anomaly volume transport calculations, results in an absolute SB volume transport of 1.4 ± 1.7 Sv in winter 2014/15 (DJF) and 1.9 ± 1.2 Sv in winter 2015/16.

Low-pressure systems approaching Svalbard and the Barents Sea from the south show an increased impact on the wind patterns during autumn and winter (Wickström et al., 2020). Moreover, it has been shown that the number of cyclones influencing Svalbard has increased during winter over the last four decades (Rogers et al., 2005; Wickström et al., 2020). Figure 18 shows that the transport across the YP can increase by up to 0.4 Sv in the SPC and 2 Sv in the SB in the winter period when the average temperature in the northward-flowing AW is close to the highest temperature in this region (Figure 9). This has a major impact on the water masses and sea ice cover north of Svalbard. Onarheim et al. (2014) have shown that the largest sea ice loss was found during the early winter months (DJF) which was explained by the increased heat content of the AW in the WSC. However, as shown here, the wind forcing events taking place over the YP and the WSS (on time scales of days and weeks) are important factors controlling the northward advection of AW in the shortest pathway of AW over the YP, the SB. It is therefore crucial to represent the spatial wind pattern in this region correctly to capture the true ocean response through the wind stress curl forcing. Seasonal variability in the SB is not captured by the latest model simulations (Crews et al., 2019; Koenig et al., 2017; Wekerle et al., 2017) that focus on the branching of the AW flow across and around the YP, and one of the reasons could be a lack of spatial resolution in the wind forcing, and hence, a wrong representation of the wind stress curl forcing of the water column over the YP. Here, the use of NORA10 wind stress data has shown that there is a high correlation between the wind stress curl pattern over the YP (and upstream along the WSS) and the seasonal and interannual volume transport anomalies in the SPC and the SB. A realistic estimate of the heat flux into the Arctic Ocean is crucially dependent on a reliable AW volume transport estimate across the YP.

On the YP, the water column is dominated by AW during the winter months, which results in a seasonal maximum heat transport also during winter. During the last decade, the water temperature in the SPC has warmed during winter due to flooding of AW onto the WSS (F. Nilsen et al., 2016), making the SPC a heat source for the melting sea ice cover in northern Svalbard, both on the shelf and in the fjords (Skogseth et al., 2020). Here we have been able to quantify the heat flux controlled by the anomalous flow (Figure 19)

to above 3 TW. However, since the mean SPC flow is not known in the Yermak Section, it is not possible to account for the mean advection of the large anomalous temperature difference seen in Figure 19a for winter 2015/16. Due to the mean SB velocity determined by altimetry in the Yermak Section, it was however possible to estimate the total heat transport anomaly in the SB and its effect on the northern side of Svalbard. A peak of more than 10 TW was calculated (Figure 20a) in connection to the strong windstorm named "Frank" (Kim et al., 2017) in January 2016. Furthermore, it was possible to separate the absolute heat flux into different terms that can explain the effect of the flow and temperature fluctuations: (a) fluctuating transport of the mean temperature difference $v'_b \overline{\delta T}$, (b) the mean transport of fluctuating temperature difference $v_0 \delta T'$, and (c) the fluctuating transport of the fluctuating temperature difference $v'_b \delta T'$. Note that the seasonal temperature difference $dT = T - T_m = \overline{\delta T} + \delta T'$ between the YP and the study box north of Svalbard (confined to the SB) was constructed from our 2-year vertically averaged hydrographic time series at YPC adjusted by a cooling rate of $\overline{\delta T} = 0.3°C$, based on historical data from the study area (Skogseth et al., 2019). Nonetheless, term (a) tends to be large for strong windstorm events in winter and give a short-period "weather" response, while term (b) is more linked to interannual variations and long-time changes in water mass temperature on the YP with a "climatic" effect on the heat transport. Hence, as also reported in Onarheim et al. (2014) and Muilwijk et al. (2018), we find that the variations in AW temperature could dominate long-time climatic trends in the heat transport into the Arctic Ocean. However, the large and short-period changes in the volume transport across the YP, due to air-ocean interaction dynamics, could govern the changes in water mass composition and sea ice cover north of Svalbard on a daily to seasonal time scale. As a consequence of the latter, and with a shift in the atmospheric circulation pattern toward an increasing number of cyclones influencing Svalbard during winter (Rogers et al., 2005; Wickström et al., 2020), the heat transport term (a) controlled by the volume flux variation will amplify the warming trend during years with anomalous atmospheric circulation patterns. Finally, the eddy correlation term (c) contains the anomaly heat transport from long-period oscillations (14 days to a month) that can exist on the YP given the right conditions (Ersdal, 2020). As a result, the sum of these three terms will either amplify or dampen down the total heat flux time series on a short or long time scale, and make the interannual variability of the heat transport in the SB larger.

Data Availability Statement

The data are published in the Norwegian Centre for Research Data (Nilsen, 2019). Matlab toolbox provided by Lilly, J. M. (2019), jLab: A data analysis package for Matlab, v. 1.6.6, http://www.jmlilly.net/jmlsoft.html.

References

Aaboe, S., & Nøst, O. A. (2008). A diagnostic model of the Nordic seas and Arctic Ocean circulation: Quantifying the effects of a variable bottom density along a sloping topography. *Journal of Physical Oceanography*, *38*, 2685–2703. https://doi.org/10.1175/2008JPO3862.1

Aagaard, K., Foldvik, A., & Hillman, S. R. (1987). The west Spitsbergen current: Disposition and water mass transformation. *Journal of Geophysical Research*, *92*(C4), 3778–3784. https://doi.org/10.1029/jc092ic04p03778

Årthun, M., Eldevik, T., Viste, E., Drange, H., Furevik, T., Johnson, H. L., & Keenlyside, N. S. (2017). Skillful prediction of northern climate provided by the ocean. *Nature Communications*, *8*(1), 15875. https://doi.org/10.1038/ncomms15875

Berge, J., Johnsen, G., Nilsen, F., Gulliksen, B., & Slagstad, D. (2005). Ocean temperature oscillations causes the reappearance of blue mussels in Svalbard after 1,000 years of absence. *Marine Ecology Progress Series*, *303*, 167–175. https://doi.org/10.3354/meps303167

Beszczynska-Möller, A., Fahrbach, E., Schauer, U., & Hansen, E. (2012). Variability in Atlantic water temperature and transport at the entrance to the arctic ocean, 1997–2010. *ICES Journal of Marine Science: Journal du Conseil*, *69*, 852–863. https://doi.org/10.1093/icesjms/fss056

Bourke, R. H., Weigel, A. M., & Paquette, R. G. (1988). The westward turning branch of the west Spitsbergen current. *Journal of Geophysical Research*, *14*, 14065–14077. https://doi.org/10.1029/jc093ic11p14065

Cokelet, E. D., Tervalon, N., & Bellingham, J. G. (2008). Hydrography of the west Spitsbergen current, Svalbard branch: Autumn 2001. *Journal of Geophysical Research*, *113*. https://doi.org/10.1029/2007JC004150

Cottier, F., Nilsen, F., Inall, M., Gerland, S., Tverberg, V., & Svendsen, H. (2007). Wintertime warming of an Arctic shelf in response to large-scale atmospheric circulation. *Geophysical Research Letters*, *34*, L10607. https://doi.org/10.1029/2007GRL029948

Crews, L., Sundfjord, A., & Hattermann, T. (2019). How the Yermak pass branch regulates Atlantic water inflow to the Arctic Ocean. *Journal of Geophysical Research: Oceans*, *124*(1), 267–280. https://doi.org/10.1029/2018JC014476

Ersdal, E. A. (2020). *Ocean motion on the Yermak Plateau (Unpublished doctoral dissertation)*. The University Centre in Svalbard (UNIS) and University of Bergen.

Fer, I., Müller, M., & Peterson, A. K. (2015). Tidal forcing, energetics, and mixing near the Yermak Plateau. *Ocean Science*, *11*, 287–304. https://doi.org/10.5194/os-11-287-2015

Fer, I., Skogseth, R., & Geyer, F. (2010). Internal waves and mixing in the marginal ice zone near the Yermak plateau. *Journal of Physical Oceanography*, *40*(7), 1613–1630. https://doi.org/10.1175/2010JPO4371.1

Francis, J. A., & Vavrus, S. J. (2012). Evidence linking arctic amplification to extreme weather in mid-latitudes. *Geophysical Research Letters*, *39*, L06801. https://doi.org/10.1029/2012GL051000

Gascard, J. C., Richez, C., & Rouault, C. (1995). Coastal and estuarine studies. In W. Smith, & J. Grebmeier (Eds.), *Arctic oceanography: Marginal ice zones and continental shelves* (Vol. 49, pp. 131–182). AGU. https://doi.org/10.1029/ce049p0131

González-Pola, C., Larsen, K. M. H., Fratantoni, P., Beszczynska-Möller, A., & Hughes, S. L. (2018). *Ices report on ocean climate 2016* (p. 339). ICES Cooperative Research.

Hanssen-Bauer, I., Førland, E. J., Hisdal, H., Mayer, S., Sandø, A. B., & Sorteberg, A. (2019). *Climate in Svalbard 2100—A knowledge base for climate adaptation*. Norsk klimaservicesenter (NKSS)/Norwegian Centre for Climate Services (NCCS).

Hattermann, T., Isachsen, P. E., Von Appen, W.-J., Albretsen, J., & Sundfjord, A. (2016). Edyy-driven recirculation of Atlantic water in Fram strait. *Geophysical Research Letters*, *43*(12), 3406–3414. https://doi.org/10.1002/2016GL068323

Hegseth, E. N., & Tverberg, V. (2013). Effect of Atlantic water inflow on the timing of the phytoplankton spring bloom in a high arctic fjord (Kongsfjorden, Svalbard). *Journal of Marine Systems*, *113–114*, 94–105. https://doi.org/10.1016/j.jmarsys.2013.01.003

Helland-Hansen, B., & Nansen, F. (1909). The Norwegian Sea. Its physical oceanography based upon the Norwegian Researches 1900-1904. *Report on Norwegian Fishery and Marine Investigations*, *11*(2), 1–359.

Hunkins, K. (1986). Anomalous diurnal tidal currents on the Yermak plateau. *Journal of Marine Research*, *44*(1), 51–69. https://doi.org/10.1357/002224086788460139

Ivanov, V., Alexeev, V., Koludnov, N. V., Repina, I., Sandø, A. B., Smedsrud, L. H., & Smirnov, A. (2016). Arctic Ocean heat impact on regional ice decay: A suggested positive feedback. *Journal of Physical Oceanography*, *36*, 1437–1456. https://doi.org/10.1175/JPO-D-15-0144.1

Jakobsson, M. (2002). Hypsometry and volume of the Arctic Ocean and its constituent seas. *Geochemistry, Geophysics, Geosystems*, *3*(2), 1–18. https://doi.org/10.1029/2001GC000302

Kim, B.-M., Hong, J.-Y., Jun, S.-Y., Zhang, X., Kwon, H., Kim, S.-J., et al. (2017). Major cause of unprecedented arctic warming in January 2016: Critical role of an Atlantic windstorm. *Scientific Reports*, *7*, 40051. https://doi.org/10.1038/srep40051

Koenig, Z., Provost, C., Sennéchael, N., Garric, G., & Gascard, J.-C. (2017). The Yermak pass branch: A major pathway for the Atlantic water north of Svalbard? *Journal of Geophysical Research: Oceans*, *122*(12), 9332–9349. https://doi.org/10.1002/2017JC013271

Langehaug, H., Sandø, A. B., Årthun, M., & Ilicak, M. (2018). Variability along the Atlantic water pathway in the forced Norwegian Earth system model. *Climate Dynamics*, *52*, 1211–1230. https://doi.org/10.1007/s00382-018-4184-5

Langehaug, H. R., & Falck, E. (2012). Changes in the properties and distribution of the intermediate and deep waters in the Fram strait. *Progress in Oceanography*, *96*(2), 57–76. https://doi.org/10.1016/j.pocean.2011.10.002

Large, W. G., & Pond, S. (1981). Open ocean momentum flux measurements in moderate to strong winds. *Journal of Physical Oceanography*, *11*(3), 324–336. https://doi.org/10.1175/1520-0485(1981)011<0324:oomfmi>2.0.co;2

Lee, T., Fukumori, I., & Tang, B. (2004). Temperature advection: Internal versus external processes. *Journal of Physical Oceanography*, *34*, 1936–1944. https://doi.org/10.1175/1520-0485(2004)034<1936:taivep>2.0.co;2

Loeng, H. (1991). Features of the physical oceanographic conditions of the Barents sea. *Polar Research*, *10*, 5–18. https://doi.org/10.3402/polar.v10i1.6723

Manley, T., Bourke, R., & Hunkins, K. (1992). Near-surface circulation over the Yermak plateau in northern Fram strait. *Journal of Marine Systems*, *3*(1–2), 107–125. https://doi.org/10.1016/0924-7963(92)90033-5

Morison, J. (1991). Seasonal variations in the west Spitsbergen current estimated from bottom pressure measurements. *Journal of Geophysical Research: Oceans*, *96*(C10), 18381–18395. https://doi.org/10.1029/91jc01916

Muckenhuber, S., Nilsen, F., Korosov, A., & Sandven, S. (2016). Sea ice cover in Isfjorden and Hornsund, Svalbard (2000–2014) from remote sensing data. *The Cryosphere*, *10*, 149–158. https://doi.org/10.5194/tc-10-149-2016

Muilwijk, M., Smedsrud, L. H., Ilicak, M., & Drange, H. (2018). Atlantic water heat transport variability in the 20th century Arctic Ocean from a global ocean model and observations. *Journal of Geophysical Research: Oceans*, *123*, 8159–8179. https://doi.org/10.1029/2018JC014327

Nilsen, F. (2019). *Remote sensing of ocean circulation and environmental changes (REOCIRC) [Data set]*. NSD—Norwegian Centre for Research Data. https://doi.org/10.18712/nsd-nsd2756-v1

Nilsen, F., Cottier, F., Skogseth, R., & Mattsson, S. (2008). Fjord-shelf exchanges controlled by ice and brine production: The interannual variation if Atlantic Water in Isfjorden, Svalbard. *Continental Shelf Research*, *28*, 1838–1853. https://doi.org/10.1016/j.csr.2008.04.015

Nilsen, F., Skogseth, R., Vaardal-Lunde, J., & Inall, M. (2016). A simple shelf circulation model: Intrusion of Atlantic water on the west Spitsbergen shelf. *Journal of Physical Oceanography*, *46*, 1209–1230. https://doi.org/10.1175/JPO-D-15-0058.1

Nilsen, J. E., Hátún, H., Mork, K., & Valdimarsson, H. (2008). *The NISE dataset (no. 08-01)*. Faroese Fisheries Laboratory. https://doi.org/10.13140/RG.2.1.3097.944

Onarheim, I. H., Smedsrud, L. H., Ingvaldsen, R. B., & Nilsen, F. (2014). Loss of sea ice during winter north of Svalbard. *Tellus*, *66*(23933). https://doi.org/10.3402/tellusa.v66.23933

Padman, L., Plueddemann, A. J., Muench, R. D., & Pinkel, R. (1992). Diurnal tides near the Yermak plateau. *Journal of Geophysical Research: Oceans*, *97*(C8), 12639–12652. https://doi.org/10.1029/92jc01097

Pavlov, A. K., Tverberg, V., Ivanov, B. V., Nilsen, F., Falk-Petersen, S., & Granskog, M. A. (2013). Warming of Atlantic water in two west Spitsbergen fjords over the last century (1912–2009). *Polar Research*, *32*(11206), 14. https://doi.org/10.3402/polar.v32i0.11206

Polyakov, I. V., Pnyushkov, A. V., Alkire, M. B., Ashik, I. M., Baumann, T. M., Carmack, E. C., et al. (2017). Greater role for Atlantic inflows on sea-ice loss in the Eurasian basin of the Arctic Ocean. *Science*, *356*(6335), 285–291. https://doi.org/10.1126/science.aai8204

Pugh, D., & Woodworth, P. (2014). *Sea-level science: Understanding tides, surges, tsunamis and mean sea-level changes* (2nd ed.). Cambridge University Press.

Quadfasel, D., Gascard, J.-C., & Koltermann, K. P. (1987). Large-scale oceanography in Fram strait during the 1984 marginal ice-zone experiment. *Journal of Geophysical Research*, *92*, 6719–6728. https://doi.org/10.1029/jc092ic07p06719

Reeve, M. A., & Kolstad, E. W. (2011). The Spitsbergen south cape tip jet. *Quarterly Journal of the Royal Meteorological Society*, *137*, 1739–1748. https://doi.org/10.1002/qj.876

Reistad, M., Breivik, O., Haakenstad, H., Aarnes, O., Furevik, B., & Bidlot, J.-R. (2011). A high-resolution hindcast of wind and waves for the North Sea, the Norwegian Sea, and the Barents Sea. *Journal of Geophysical Research*, *16*, 2685–2703. https://doi.org/10.1029/2010jc006402

Rogers, J. C., Yang, L., & Li, L. (2005). The role of Fram strait winter cyclones on sea ice flux and on Spitsbergen air temperatures. *Geophysical Research Letters*, *32*, L06709. https://doi.org/10.1029/2004GL022262

Saloranta, T. M., & Haugan, P. M. (2004). Northward cooling and freshening of the warm core of the west Spitsbergen current. *Polar Research*, *23*(1), 79–88. https://doi.org/10.3402/polar.v23i1.6268

Sandvik, A. D., & Furevik, B. R. (2002). Case study of a coastal jet at Spitsbergen—Comparison of SAR- and model-estimated wind. *Monthly Weather Review*, *130*, 1040–1051. https://doi.org/10.1175/1520-0493(2002)130<1040:csoacj>2.0.co;2

Schauer, U., & Beszczynska-Möller, A. (2009). Problems with estimation and interpretation of oceanic heat transport: Conceptual remarks for the case of Fram strait in the Arctic Ocean. *Ocean Science*, *5*, 487–494. https://doi.org/10.5194/os-5-487-2009

Serreze, M., & Barry, R. (2011). Processes and impacts of Arctic amplification: A research synthesis. *Global and Planetary Change*, *77*(1–2), 85–96. https://doi.org/10.1016/j.gloplacha.2011.03.004

Skogseth, R., Ellingsen, P., Berge, J., Cottier, F., Falk-Petersen, S., Ivanov, B., & Vader, A. (2019). *Unis hydrographic database [data set]*. Norwegian Polar Institute. https://doi.org/10.21334/unis-hydrography

Skogseth, R., Olivier, L., Nilsen, F., Falck, E., Fraser, N., Tverberg, V., & Falk-Petersen, S. (2020). Variability and decadal trends in the Isfjorden (Svalbard) ocean climate and circulation—An indicator for climate change in the European arctic. *Progress in Oceanography*, *187*, 102394. https://doi.org/10.1016/j.pocean.2020.102394

Stroeve, J. C., Serreze, M. C., Holland, M. M., Kay, J. E., Maslanik, J., & Barrett, A. P. (2012). The Arctic's rapidly shrinking sea ice cover: A research synthesis. *Climate Change*, *110*, 1005–1027. https://doi.org/10.1007/s10584-011-0101-1

Svendsen, H., Beszczynska-Møller, A., Hagen, J. O., Lefauconnier, B., Tverberg, V., Gerland, S., & Dallmann, W. (2002). The physical environment of Kongsfjorden-Krossfjorden, an Arctic fjord system in Svalbard. *Polar Research*, *21*(1), 133–166. https://doi.org/10.3402/polar.v21i1.6479

Swift, J. H., & Aagaard, K. (1981). Seasonal transitions and water mass formation in the Iceland and Greenland Sea. *Deep-Sea Research*, *28*, 1107–1129. https://doi.org/10.1016/0198-0149(81)90050-9

Teigen, S. H., Nilsen, F., Skogseth, R., Gjevik, B., & Beszczynska-Möller, A. (2011). Baroclinic instability in the west Spitsbergen current. *Journal of Geophysical Research*, *116*, C07012. https://doi.org/10.1029/2011JC006974

Tverberg, V., Nøst, O. A., Lydersen, C., & Kovacs, K. M. (2014). Winter sea ice melting in the Atlantic water subduction area, Svalbard Norway. *Journal of Geophysical Research: Oceans*, *119*. https://doi.org/10.1002/2014JC010013

Tverberg, V., Skogseth, R., Cottier, F., Sundfjord, A., Walczowski, W., Inall, M., & Nilsen, F. (2019). The Kongsfjorden transect: Seasonal and inter-annual variability in hydrography. In H. Hop, & C. Weincke (Eds.), *Advances in polar ecology*. Springer Verlag. https://doi.org/10.1007/978-3-319-46425-1_3

Uppala, S., Kållberg, P., Simmons, A., Andreae, U., Da Costa Bechtold, V., Fiorino, M., & Woolen, J. (2005). The era-40 re-analysis. *Quarterly Journal of the Royal Meteorological Society*, *131*, 2961–3012. https://doi.org/10.1256/qj.04.176

von Appen, W., Schauer, U., Hattermann, T., & Beszczynska-Möller, A. (2016). Seasonal cycle of mesoscale instability of the west Spitsbergen current. *Journal of Physical Oceanography*, *46*, 1231–1254. https://doi.org/10.1175/JPO10.1175/jpo-d-15-0184.1

Wekerle, C., Wang, Q., von Appen, W.-J., Danilov, S., Schourup-Kristensen, V., & Jung, T. (2017). Eddy-resolving simulation of the Atlantic water circulation in the Fram strait with focus on the seasonal cycle. *Journal of Geophysical Research: Oceans*, *122*. https://doi.org/10.1002/2017JC012974

Wickström, S., Jonassen, M., Vihma, T., & Uotila, P. (2020). Trends in cyclones in the high latitude north Atlantic during 1979–2016. *The Quarterly Journal of the Royal Meteorological Society*, *146*, 762–779. https://doi.org/10.1002/qj.3707

Wunsch, C., & Stammer, D. (1997). Atmospheric loading and oceanic "inverted barometer" effect. *Reviews of Geophysics*, *35*(1). https://doi.org/10.1029/96RG03037